Load Model Complexity Analysis and Real-Time Load Tracking (S-60)

Final Project Report

S-60

Power Systems Engineering Research Center

*Empowering Minds to Engineer
the Future Electric Energy System*

Load Model Complexity Analysis and Real-Time Load Tracking (S-60)

Final Project Report

Project Team

Hao Zhu, Project Leader
Thomas Overbye
University of Illinois at Urbana-Champaign

Bernie Lesieutre
University of Wisconsin-Madison

Graduate Students

Siming Guo
University of Illinois at Urbana-Champaign

Kaiqing Zhang
University of Illinois at Urbana-Champaign

For information about this project, contact

Hao Zhu
University of Illinois at Urbana-Champaign
Department of Electrical and Computer Engineering
4056 ECE Building
306 North Wright St. Urbana, IL, 61801
haozhu@illinois.edu

Power Systems Engineering Research Center

The Power Systems Engineering Research Center (PSERC) is a multi-university Center conducting research on challenges facing the electric power industry and educating the next generation of power engineers. More information about PSERC can be found at the Center's website: http://www.pserc.org.

For additional information, contact:

Power Systems Engineering Research Center
Arizona State University
527 Engineering Research Center
Tempe, Arizona 85287-5706
Phone: 480-965-1643
Fax: 480-965-0745

Acknowledgements

Executive Summary

Power system dynamic simulations and transient stability studies vitally depend on the accuracy of the load models. However, it is widely recognized that the monitoring capability for loads is insufficient while the accuracy of load models has not been fully investigated. Meanwhile, the analysis on the adequacy or necessity of existing dynamic composite load models is left open the literature. This project aims to tackle these challenging by analyzing the complexity trade-off of the load models used for studying the increasingly critical fault-induced delayed-voltage recovery (FIDVR) events. Real-time and non-intrusive estimation of the load models are also pursued in this project, by leveraging high-resolution and high-bandwidth data even available within distribution feeders. This project has successfully developed a software tool for grid operators to perform measurement-based load modeling using the WECC composite load model (CMPLDW) structure. The report is presented in two parts.

Part I: Model Complexity Analysis and Improved Parameter Estimation for Dynamic Load Models

Transient stability analysis is becoming increasingly important for power systems engineers and researchers. Accurate dynamic models are required, but dynamic load modeling by fitting the input-output measurements during fault events is an area of weakness. For example, the WECC composite load model (CMPLDW) has been developed recently as an improvement to existing composite load models such as the complex load model (CLOD). The WECC CMPLDW has been developed to better represent fault-induced delayed-voltage-recovery (FIDVR) events, which are of increasing concern to electric utilities. However, the model nonlinearity and large number of parameters of the WECC CMPLDW model pose severe identifiability issues and performance degradation for the measurement-based load modeling approach using the classical nonlinear least-squares (NLS) objective.

This report will first present a general framework that can effectively analyze and visualize the parameter (in)sensitivity and dependency of complex dynamic load models with large numbers of parameters under FIDVR. The possible impact of these effects on the predictive ability of the model is also explored. Finally, we present an improved parameter estimation algorithm by better designing the NLS error objective using a regularized term according to *a priori* information on parameter values. Two different types of regularization techniques have been proposed. Effectiveness of our model sensitivity and dependency analysis, as well as the improved numerical performance of the proposed parameter estimation schemes, have been validated using both synthetic data and real measurement collected during FIDVR events. Albeit focused on the WECC CMPLDW and the CLOD model, the proposed approaches can be readily used for dynamic composite load modeling in general.

Part II: Non-intrusive Load Monitoring within Distribution Feeders

The FIDVR phenomenon is believed to be driven by the stalling of single-phase compressor motors, such as those in residential air conditioners and refrigerators. While CMPLDW was specifically designed to replicate this behavior, it may still be inadequate due to being a positive sequence model. Positive sequence simulations assume that sub-cycle phenomena are negligible,

but we show in both simulation and laboratory testing that this is not true for compressor motors. For an instantaneous voltage drop event, the motor is much more likely to stall if the event occurs at the moment of zero crossing as opposed to at a peak.

One aspect of load modeling that is often discussed but unsolved is the real-time updating of load model parameters on a daily or seasonal basis. In this work, we propose using harmonic information to monitor load composition. For example, the often-observed "rabbit ears" are characteristic of a power electronic load with a rectified front-end. Based on empirical data measured at an office building, we can observe that such loads are active during the day, but absent at night, which suggests an HVAC system run by variable frequency drives. Based on such analysis at the aggregate level, we can perform long term monitoring of load dynamics.

Project Publications:

K. Zhang, H. Zhu, and S. Guo, "Dependency analysis and improved parameter estimation for dynamic composite load modeling," *IEEE Transactions on Power Systems*, 2017 (accepted). [Online] http://ieeexplore.ieee.org/abstract/document/7728116/

K. Zhang, S. Guo, and H. Zhu, "Parameter sensitivity and dependency analysis for the WECC dynamic composite load model," *Proc. of 47th Hawaii Intl. Conf. on System Sciences (HICSS)*, Jan. 2017. [Online] http://scholarspace.manoa.hawaii.edu/handle/10125/41540
S. Guo, K. S. Shetye, T. J. Overbye, and H. Zhu, "Impact of measurement selection on load model parameter estimation," *Proc. of Power and Energy Conference at Illinois (PECI)*, Feb. 2017.

Student Thesis:

S. Guo, "Improvements to power system dynamic load model parameter estimation," Ph.D. dissertation, Dept. Elec. Eng., Univ. Illinois at Urbana-Champaign, Urbana, IL, 2017.

Contents

List of Figures

List of Tables

Part I

University of Illinois at Urbana-Champaign

Chapter 1

Introduction

Development of dynamic load models is essential for transient stability analysis and control designs in power systems [1,2]. However, due to the inherent uncertainty, complexity, and diversity of power system loads, their modeling remains challenging to academic and industrial researchers [3]. Thanks to wide deployment of digital fault recorders, the measurement-based load modeling approach becomes increasingly popular; see [4–9]. This approach determines parameters of a given model structure by fitting field measurements during system disturbances, and the resultant parameterized models can be directly used for dynamic studies.

There exist several dynamic load model structures for measurement-based load modeling. One popular choice consists of a static constant impedance-current-power (ZIP) component and a dynamic induction motor (IM) component. This ZIP+IM model has been widely used due to its simple structure [4–7]. In addition, the complex load model (CLOD) developed by PSS/E, which has been preliminarily investigated in [8], has several more components including two IMs of different torque-speed and current-speed curves. Although these load models are effective in representing load dynamic behavior during most short-duration faults, they fail to model fault-induced delayed-voltage-recovery (FIDVR) events; see [10, 11]. Slow voltage recovery after low-voltage faults is mainly caused by the stalling of low-inertia single-phase IMs. It is of increasing concern to utilities because of the resultant loss of voltage control and potential cascading effects. To model FIDVR events, the WECC composite load model (CMPLDW) has been developed [9], which includes a single-phase IM component among other enhancements. There exist very few studies on measurement-based load modeling using CMPLDW.

The CMPLDW model, or general composite load models, are known for having a large number of input parameters and being nonlinear. The resultant parameter identifiability issues challenge the measurement-based load modeling. Even for the CLOD model of just a few parameters, it has been observed in [8] that the fraction of large or small IMs could contribute equally to the dynamic load response. Dependency of these two fraction parameters implies they cannot be uniquely identified using the input-output measurements. Similar parameter dependency effect has been observed for the ZIP+IM model as well [6]. To investigate potential parameter dependency for CMPLDW, we propose to adopt the K-medoids algorithm [12] to cluster the model parameters, as well as to use the multidimensional scaling (MDS) technique [13] to visualize the parameter similarity. Unlike [6] which only considers the pair-wise correlation of any two parameters, our

proposed approach can capture the dependency among multiple parameters, more attractive for dealing with the large number of CMPLDW parameters.

Model interdependency negatively impacts the parameter estimation, and often this results in an estimate from the training case which is optimal but unreasonable. The consequences of this unidentifiability are then analyzed, by examining the performance of the model solution on previously unseen test cases. The effect of increasing the number of training cases is also examined.

Results from the first five chapters motivate us to improve the estimation scheme for load model parameters using fault measurements. This problem is typically formulated as nonlinear least-squares (NLS) by minimizing the fitting error between the modeled and measured outputs. To tackle this ill-posed problem due to parameter dependency, we advocate to incorporate *a priori* information in the parameter estimation. Two methods are presented. The first uses a maximum a-posteriori (MAP) estimation method, and the second uses a 2-norm based regularization term. To the best of our knowledge, no previous work has leveraged the regularization technique to overcome the identifiability issues in measurement-based load modeling. Although our improved estimation scheme will focus on CLOD and CMPLDW, it can readily used for other dynamic load models as well.

This report is organized as follows. Chapter 2 introduces the CMPLDW and CLOD models and the background on measurement-based load modeling. Chapter 3 presents the sensitivity analysis of the CMPLDW model. Chapter 4 presents the analysis and visualization of the dependency among CMPLDW parameters. The consequences of parameter insensitivity and interdependency is presented in Chapter 5. Two improved parameter estimation approaches are developed and validated in Chapter 6. Concluding remarks are addressed in Chapter 7.

Chapter 2

Modeling and Problem Statement

This work is focused on the composite WECC CMPLDW and complex load (CLOD) structures and the modeling of FIDVR events.

2.1 WECC CMPLDW

Fig. 2.1 illustrates the structure of the model. It consists of a substation transformer model, a feeder equivalent model, and six load model components [9]. The load components include three three-phase (3Φ) motors, one single-phase (1Φ) motor, one static ZIP load, and an electronic load, all connected in parallel. The 3Φ motors are henceforth named motor A, B, and C, and the 1Φ motor, which is used to model an air conditioner compressor, is named motor D. Compared to the simple ZIP+IM model of only 13 parameters [5], the WECC CMPLDW model has a more extensive list of parameters used to describe its static and dynamic behaviors under disturbances. A representative CMPLDW model has in total 121 parameters as listed in Table 2.1; see more detailed in [9]. Table 2.1 also shows example parameter values, developed by an earlier report [10]. These parameters can be categorized to represent the following:

- substation and feeder (e.g., transformer reactance and feeder equivalent impedance);

- load model components (e.g., reactance and inertia of a motor, or the ZIP coefficients);

- the fraction for each load component (e.g., Fel, FmA, etc.).

We note that in the WECC CMPLDW model, a subset of them will be excluded in the ensuing study. They are marked in italic fonts in Table 2.1. Some of them either follow a fixed setting or are well known to be unidentifiable using field measurements. For instance, the induction motor type parameters MtypA, MtypB, MtypC, and MtypD as shown in Fig. 2.1, are preset to have motors A, B, and C designated as 3Φ and motor D as 1Φ. Based on the specific motor, its low voltage trip delay or reconnection time (Ttr1A, Ttr2B, or Trc2C) is often deactivated by taking an infinite value. These parameters are preset following the optimal setting in the report [10].

Table 2.1: List of WECC CMPLDW Parameters with Example Values

Feeder		Electronic Load		Motor B		Motor C		Motor D	
Bss	0	Fel	0.167	FmB	0.167	FmC	0.167	FmD	0.167
Rfdr	0.04	Pfel	1	*MtypB*	3	*MtypC*	3	*MtypD*	1
Xfdr	0.05	Vd1	0.75	LFmB	0.8	LFmC	0.8	LFmD	1
Fb	0.75	Vd2	0.65	RsB	0.03	RsC	0.03	CompPFD	0.97
Xxf	0.08	Frcel	0.25	LsB	1.8	LsC	1.8	VstallD	0.6
Tfixhs	1	Motor A		LpB	0.16	LpC	0.16	RstallD	0.1
Tfixls	1	FmA	0.167	LppB	0.12	LppC	0.12	XstallD	0.1
LTC	1	*MtypA*	3	TpoB	0.1	TpoC	0.1	TstallD	0.02
Tmin	0.9	LFmA	0.7	TppoB	0.0026	TppoC	0.0026	FrstD	0
Tmax	1.1	RsA	0.04	HB	1	HC	0.1	VrstD	0.9
step	0.00625	LsA	1.8	EtrqB	2	EtrqC	2	TrstD	0.4
Vmin	1	LpA	0.1	Vtr1B	0.5	Vtr1C	0.5	FuvrD	0.17
Vmax	1.02	LppA	0.083	Ttr1B	0.02	Ttr1C	0.02	Vtr1D	0.65
Tdel	30	TpoA	0.092	Ftr1B	0.2	Ftr1C	0.2	Ttr1D	0.02
Tdelstep	5	TppoA	0.002	Vrc1B	0.65	Vrc1C	0.65	Vtr2D	0.9
Rcmp	0	HA	0.05	Trc1B	0.6	Trc1C	0.6	Ttr2D	5
Xcmp	0	EtrqA	0	Vtr2B	0.7	Vtr2C	0.7	Vc1offD	0.4
Static Load		Vtr1A	0.75	Ttr2B	0.02	Ttr2C	0.02	Vc2offD	0.4
Pfs	-0.99	*Ttr1A*	∞	Ftr2B	0.3	Ftr2C	0.3	Vc1onD	0.45
P1e	2	Ftr1A	0.2	Vrc2B	0.85	Vrc2C	0.85	Vc2onD	0.45
P1c	0.54546	Vrc1A	0.9	*Trc2B*	∞	*Trc2C*	∞	TthD	30
P2e	1	*Trc1A*	∞					Th1tD	0.3
P2c	0.45454	Vtr2A	0.5					Th2tD	2.05
Pfrq	-1	Ttr2A	0.02					TvD	0.025
Q1e	2	Ftr2A	0.47						
Q1c	-0.5	Vrc2A	0.639						
Q2e	1	Trc2A	0.73						
Q2c	1.5								
Qfrq	-1								
MBase	0								
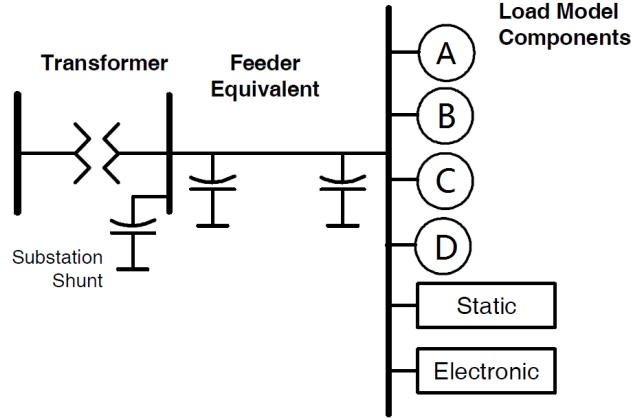
Figure 2.1: A schematic of the WECC CMPLDW composite load model [10].

2.2 CLOD

The CLOD model is a composite model defined in Siemens PSSE [14] and PowerWorld [15], which means that it combines several simpler submodels. The CLOD model contains an induction motor (IM) model, a simplified ZIP model, and a few other static components. The submodels are described in more detail here:

- **Induction motors** Labeled Large Motors and Small Motors, these two submodels are each characterized by a d-q reference frame dynamic model.

- **Discharge lighting** For voltages above 0.75 pu, the real power is modeled as constant current, and the imaginary as exponential with an exponent of 4.5. As voltage decreases below 0.75 pu, both P and Q drop linearly until the light is completely extinguished below 0.65 pu voltage.

- **Transformer losses** Transformer saturation and hysteresis losses.

- **Constant MVA** Constant real and reactive power consumption.

- **Remaining loads** The real power is modeled typically as constant current and the imaginary power as constant impedance. This is abbreviated as PI/QZ.

The CLOD model also includes a feeder with a feeder impedance. The parameters of the CLOD model are the percentage allocations of each submodel, summing to 100%. Since there are six submodels, we can set five parameters independently. Additionally, we can also set the feeder impedance, R and X, for a total of seven parameters. We chose to use the CLOD model for our studies because it contains a sufficient amount of dynamics, but is also simple enough to understand easily.

6
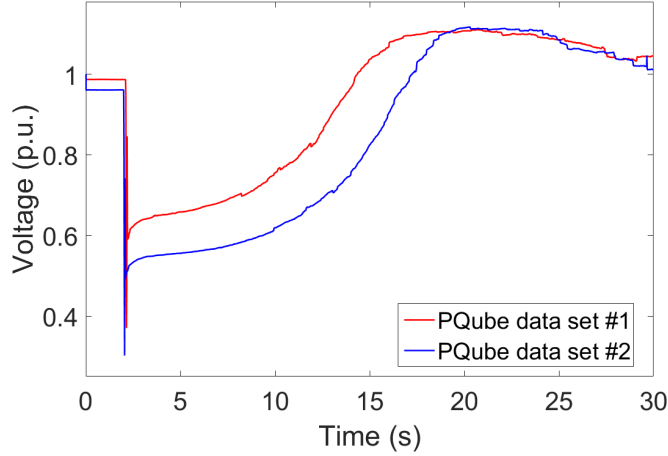
Figure 2.2: Voltage profiles during FIDVR events recorded in PQube datasets #1 and #2.

2.3 Measurement-based load modeling

With emerging fast-sampled data collected during power system disturbances, measurement-based load modeling has been advocated to effectively construct dynamic load models by estimating the model parameters. During a disturbance, fault recorders can measure the input voltage profile and the resultant real and reactive power outputs. Measurement-based load modeling aims to fit the output-measurement data via minimizing a prescribed error objective.

The data fitting objective is typically the classical Euclidean error norm. Specifically, with the output measurement vector denoted by $\mathbf{y}$, the vector of parameters $\boldsymbol{\theta}$ is estimated by solving a nonlinear least-squares problem, as given by:

$$\min_{\boldsymbol{\theta}} \frac{1}{2}\|\mathbf{r}(\boldsymbol{\theta})\|_2^2 := \frac{1}{2}\|\mathbf{y} - \mathbf{f}(\boldsymbol{\theta})\|_2^2 \tag{2.1}$$

$$\hat{\boldsymbol{\theta}} = \arg\min_{\boldsymbol{\theta}} \frac{1}{2}\|\mathbf{y} - \mathbf{f}(\boldsymbol{\theta})\|_2^2 \tag{2.2}$$

where $\mathbf{r}$ is the fitting residual based on the function $\mathbf{f}$ that relates $\boldsymbol{\theta}$ to the output. Note that the output $\mathbf{y}$ includes both real and reactive power data.

The event measurements are taken from real datasets collected by a southern US utility company. They are recorded using PQube devices [16] during three summer months in 2012. Each event includes the voltage profile and the corresponding real and reactive power consumption, all with a sampling rate of 60 Hz. Two FIDVR events have been identified from the data. As plotted in Fig. 2.2, the voltage profile of FIDVR takes a long time, usually several seconds, to recover from the voltage drop caused by a certain disturbance. This phenomenon generally results from the high penetration of single-phase induction motors in power systems, which can barely be captured by the traditional ZIP+IM model structure. We thus mainly focus on addressing FIDVR type of fault in the ensuing analysis.

7

Chapter 3

Parameter Sensitivity Analysis

As shown in [4–7], dynamic load modeling is generally challenged by the unidentifiability of parameters that describe the model structure. The unidentifiability has two primary causes: the insensitivity of some parameters and the dependency among several parameters [6]. It is difficult to identify these parameters accurately because different values of insensitive parameters or various combinations of dependent parameters may result in a similar output response. In Chapters 3 and 4, the sensitivity and interdependency of the CMPLDW parameters will be investigated. Similar analysis has been performed for the CLOD model in [17], and similar conclusions were obtained.

We will first use trajectory sensitivity analysis to obtain a feature vector for each parameter. Trajectory sensitivity represents the sensitivity of the system dynamic response to the changes of each parameter in $\boldsymbol{\theta}$ [18]. If the state-space representation of load models is available, this sensitivity factor can be evaluated using the perturbation method [4, 5]. However, for complex load models such as CMPLDW, it is difficult to develop their mathematical state-space representations. Hence, we will use a finite-difference derivative approximation to perform the trajectory sensitivity analysis. Specifically, for the i-th parameter θ_i, its trajectory sensitivity at any time t can be approximated by [18]:

$$J_i(t) := \left. \frac{\partial f(t; \boldsymbol{\theta})}{\partial \theta_i} \right|_{\boldsymbol{\theta} = \boldsymbol{\theta}_0} \approx \frac{f(t; \boldsymbol{\theta}_0 + \epsilon \mathbf{e}_i) - f(t; \boldsymbol{\theta}_0 - \epsilon \mathbf{e}_i)}{2\epsilon} \tag{3.1}$$

where $\boldsymbol{\theta}_0$ has the nominal parameter values, $\mathbf{e}_i$ is the Kronecker vector with all entries zero except for the i-th entry equal to 1, and the perturbation coefficient ϵ is a small positive value. The dynamic system output $f(t; \boldsymbol{\theta})$ under different parameter settings can be obtained by numerical simulation. Hence, the resultant sensitivity $J_i(t)$ will consist of discrete-time samples throughout the fault event. Concatenating the samples into a vector $\mathbf{J}_i$ of length T for each parameter, we can use it as the feature vector to characterize the effects of changing θ_i in the dynamic response. Note that perturbations in both active and reactive power outputs are included in the vector $\mathbf{J}_i$.

Main results from the parameters' trajectory sensitivity under FIDVR events are illustrated in this chapter. Given a fault voltage disturbance, we first show that some parameters have very minimal (even absolutely zero) sensitivity. Interestingly, we make further observations that the sensitivity is strongly related to the shape of the faulted voltage, which originates from the thresholding nonlinearity of the WECC CMPLDW.
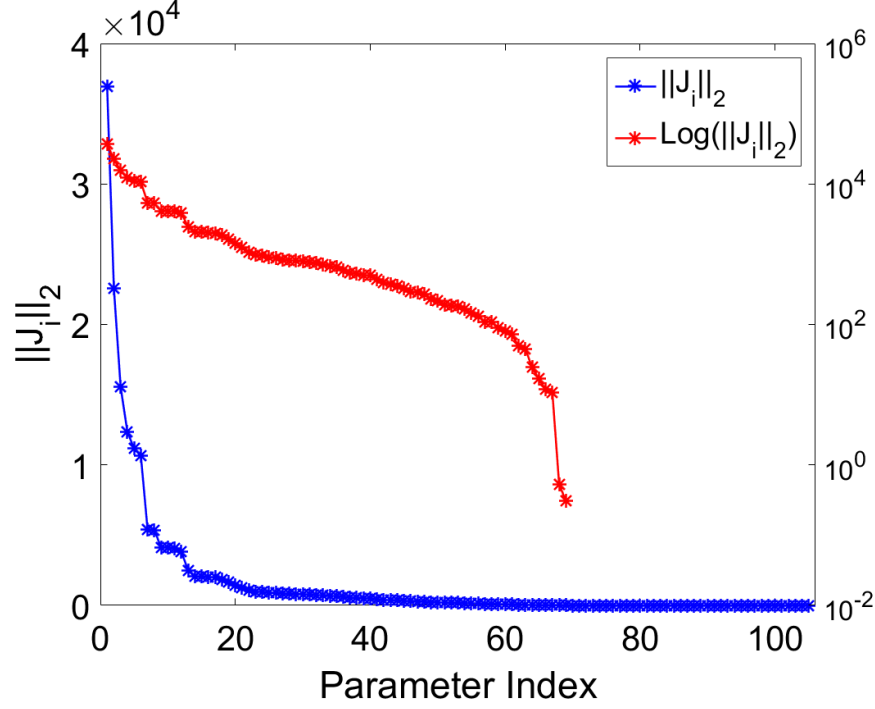
Figure 3.1: The 2-norm and its logarithm of the trajectory sensitivity of each parameter from the test on PQube data set #1, sorted in descending order.

3.1 Insensitive parameters

Using the sensitivity vectors $\{\mathbf{J}_i\}$, we can first identify the parameters that the load model output is insensitive to. Figure 3.1 plots the sorted $\|\mathbf{J}_i\|_2$ values and their logarithmic values for all CMPLDW parameters under the voltage input in dataset #1. Clearly, almost half the parameters have very minimal, or even zero, trajectory sensitivity, which means that changing the value of several CMPLDW parameters could result in negligible output perturbations. Hence, we choose a predetermined threshold $r_{th} > 0$ and only select the parameters with $\|\mathbf{J}_i\|_2 \geq r_{th}$ for the ensuing analysis. For the N parameters selected, their corresponding feature vectors are stacked into the $T \times N$ matrix $\mathbf{J}$, which is approximately the Jacobian matrix for the measurement function $\mathbf{f}(\boldsymbol{\theta})$ at $\boldsymbol{\theta} = \boldsymbol{\theta}_0$. The most significantly sensitive parameters are marked as bold in Table 2.1. Particularly, by setting the threshold r_{th} as 1% of the nominal output norm $\|\mathbf{J}_i\|_2$, a total of $N = 70$ parameters are selected to form the resultant Jacobian $\mathbf{J}$.

Some of the absolutely insensitive parameters are related to the tripping behavior of the load components, which may not be activated under the given input voltage profile. For example, parameters Vd1 and Vd2 are used to set the voltage levels for tripping the electronic load. Slightly varying their values will not cause any change of the system response if the lowest voltage input is significantly higher than the initial tripping levels specified in Vd1 and Vd2. These examples reveal the thresholding nonlinearity of the CMPLDW model. Therefore, the selection of insensitive parameters depends on both the initial parameter setting $\boldsymbol{\theta}_0$ and the input voltage profile.
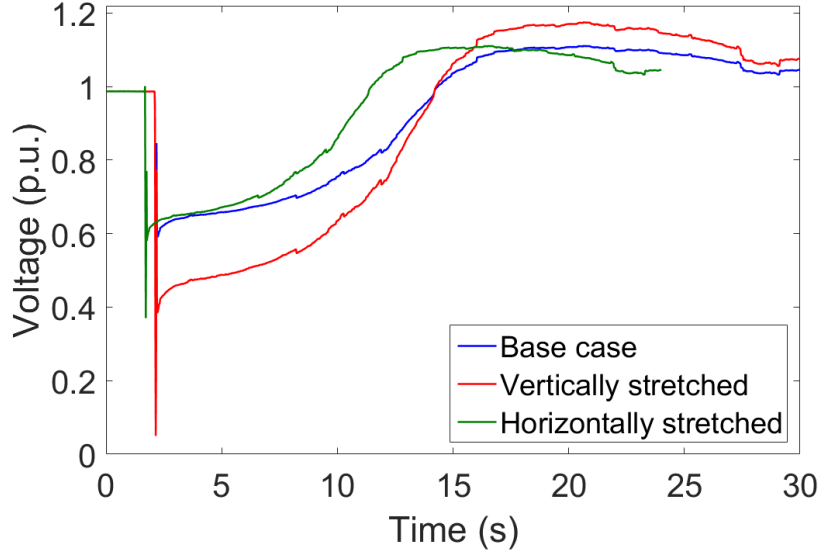
Figure 3.2: Illustration of vertical and horizontal stretching of the voltage profile.

3.2 Impact of input fault voltage profile

Building on previous analysis, we investigate the impact of the input voltage profile on the parameter sensitivity. We first designate PQube data set #1 in Figure 2.2 as our base case. We then modify the base case profile to emulate faults of varying severity and recovery time. Specifically, we scale the profile vertically to vary the minimum fault voltage, while maintaining the pre-fault voltage. We scale the profile horizontally to vary the recovery time. These are both illustrated in Figure 3.2.

The parameter sensitivities are then calculated for each voltage profile and plotted in Figure 3.3 and Figure 3.4 on a log scale. From Figure 3.3 we can see that the parameter sensitivities do not remain constant. There is a cyan colored line which has relatively low sensitivity between 0 and 0.5 p.u., peaks at 0.6 p.u., then disappears for profiles with higher minimum voltage. This line corresponds to the parameter VstallD, the stall voltage for motor D. In the base case, the stall voltage is set to 0.6 p.u.. When the minimum fault voltage does not drop below 0.6 p.u., motor D will not stall, hence VstallD does not affect the trajectory at all ($\|\mathbf{J}_i\|_2 = 0$ for VstallD). Since Figure 3.3 uses a log axis, those zero sensitivities cannot be plotted. On the other hand, when the minimum fault voltage is very close to 0.6 p.u., the sensitivity of VstallD exceeds the other parameters approximately one order of magnitude. This is because a small change in the value of VstallD will determine whether motor D stalls; this is thresholding nonlinearity. Finally, for faults where the voltage drops significantly below 0.6 p.u., motor D will definitely stall, so the trajectory again becomes very insensitive to VstallD. The reason the sensitivity is not exactly zero is merely because a more severe fault causes the voltage to drop faster, and hence causes motor D to stall a fraction of a cycle earlier.

We can also see that many parameters have a large peak in sensitivity when the minimum fault

10
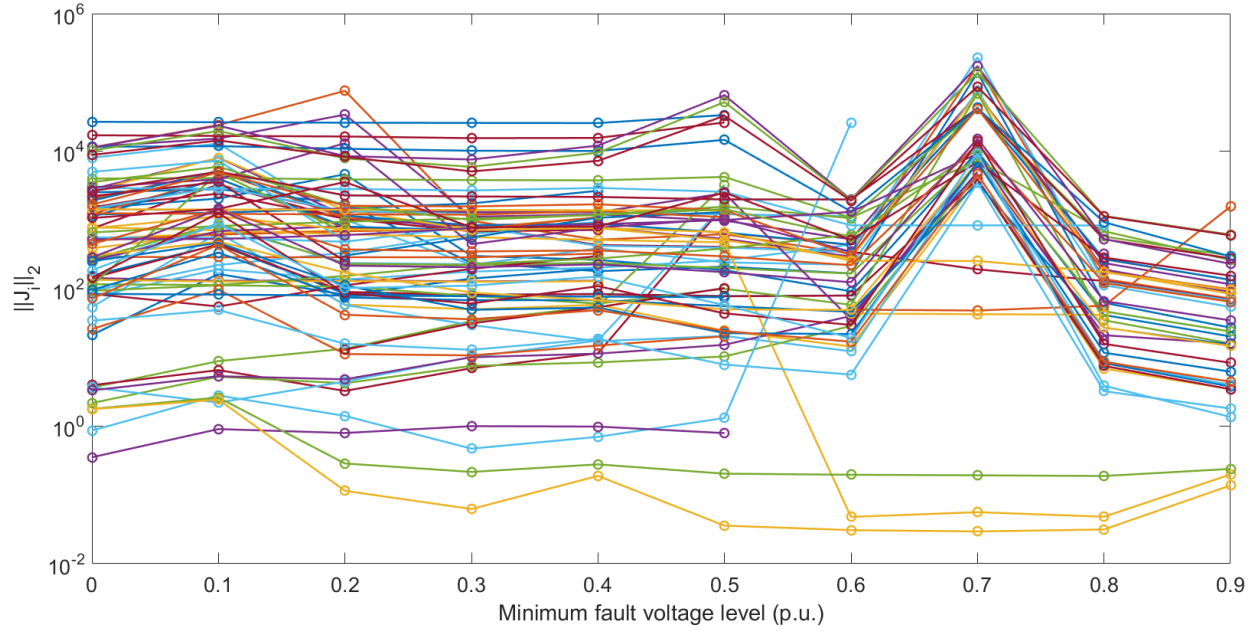
Figure 3.3: Parameter sensitivity under vertical stretching of the voltage profile. The base case minimum fault voltage level is 0.3703 pu (see Figure 2.2).
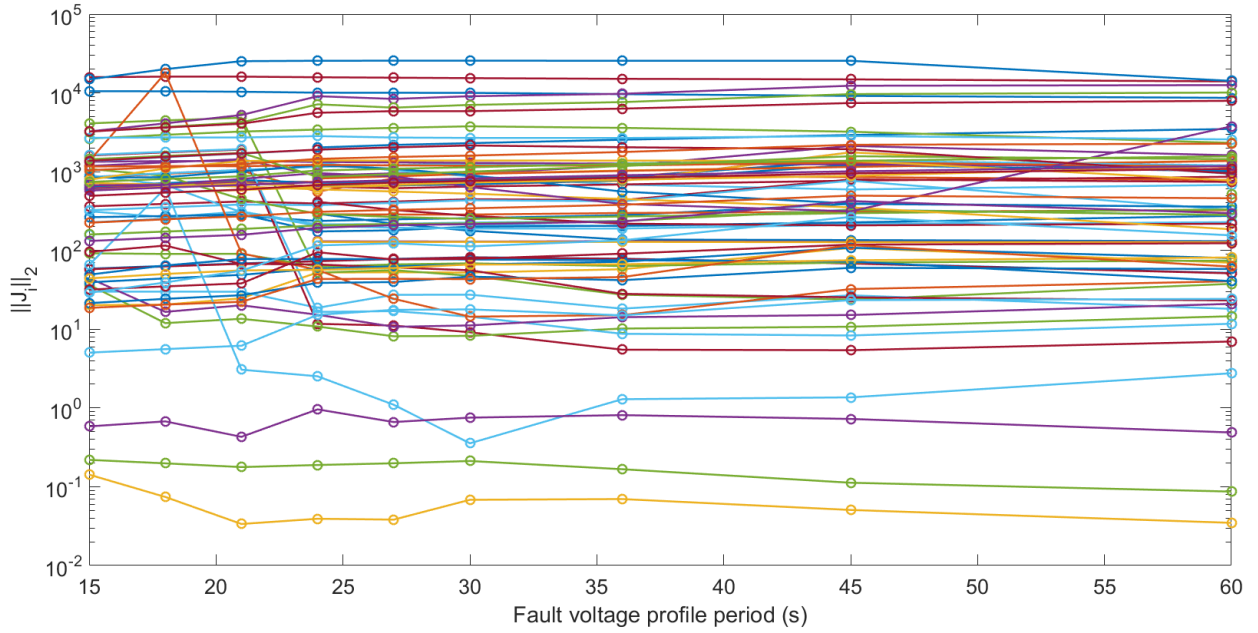
Figure 3.4: Parameter sensitivity under horizontal stretching of the voltage profile. The base case profile period is 30 s (see Figure 2.2).

voltage is 0.7 p.u. and a few parameters have a peak at 0.5 p.u.. These can also be attributed to thresholding nonlinearity. Voltage trip levels Vtr1A, Vtr2B, Vtr2C, and Vtr1D, and voltage reconnection levels Vrc1B, Vrc1C, and Vrc2A are all between 0.639 and 0.75 p.u.. Voltage trip levels Vtr1B, Vtr1C, and Vtr2A are all 0.5 p.u.. When the minimum fault voltage is near those values, not only those voltage thresholds, but also any associated time delays, such as trip delay times, become very sensitive. For example, motor B parameters Vtr1B and Ttr1B represent the under-voltage trip level and the trip delay time. If motor B does not trip for the given voltage input, varying Ttr1B will not affect the output dynamics either. The parameter sensitivities in Figure 3.4 are more uniform than those in Figure 3.3. This is because we are not affecting the minimum fault voltage. However, we still see some peaks when the profile period is reduced to around 20 s, which is evidence that thresholding non-linearity is occuring for time thresholds, such as a reconnection time delay.

Chapter 4

Parameter Dependency Analysis

Given the input-output data, it has been recognized that the estimation problem (2.1) could admit multiple (locally) optimal solutions. This observation implies that different combinations of parameter values could produce the same data fitting results in measurement-based load modeling. It has been observed for the CLOD model [8] and more rigorously studied for the ZIP+IM model [4–7].

From the perspective of systems theory, this challenge relates to the parameter identifiability issue for dynamic systems [19]. It is possible the system response is insensitive to the changes in certain parameter values. More interestingly, multiple parameters could be dependent on each other such that the system output is affected by their parameter values in an aggregated fashion. Existing studies on the parameter dependency of load models in [6] are limited to the pair-wise similarity between any two parameters. This method may work well for the simple ZIP+IM model, but falls short in studying the more complex CMPLDW with dozens of parameters. We will develop a general analysis framework that can capture the parameter dependency among multiple parameters.

4.1 Examples of dependent parameters

As an example, consider the stator resistance of motors B and C, RsB and RsC. Since the parameters of motors B and C are quite similar, we find that RsB and RsC are essentially indistinguishable from one another. In Figure 4.1, the default values of RsB and RsC (see Table 2.1) are indicated by the dashed white lines. The simulation result with RsB and RsC at their default values is the base case output. With all other parameters fixed, the values of RsB and RsC are then varied between 10% and 200% of their default value. The mean squared error (MSE) between the resulting outputs and the base case output are then calculated and contoured in the figure. From the figure, we can see that as long as RsB and RsC are varied proportionally, the MSE will stay in the dark blue region extending from the top-left to bottom-right corners. Thus, from a single set of output measurements, it is difficult to uniquely identify both RsB and RsC. Only if we pick one parameter's value can we then determine the other parameter.

While the dependence of this particular pair of parameters seems intuitive, there are other pairs of dependent parameters which have no simple explanation. Consider the following two param-
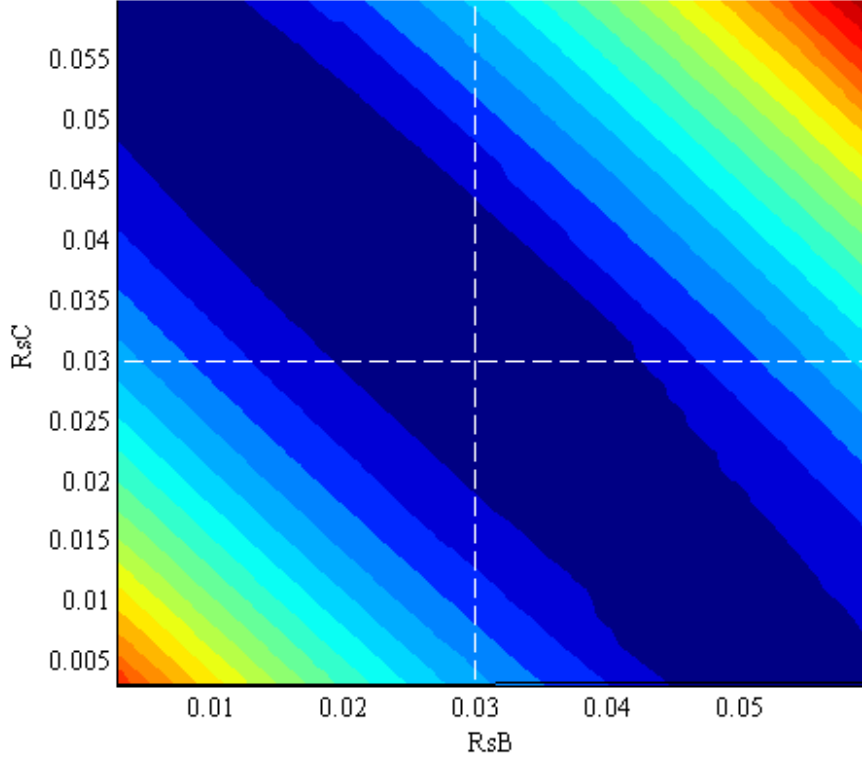
Figure 4.1: Contour of the MSE between the base case output and test cases for RsB and RsC, the stator resistances of motors B and C.

eters for the single-phase motor D: XstallD, the stall reactance in p.u., and Th2tD, the thermal protection trip completion temperature in p.u.. Both these parameters have quite high sensitivity: XstallD is ranked first, and Th2tD is 13th among all the parameters. These two parameters are also completely unrelated from a physical standpoint. However, in Figure 4.2, we can see that they exhibit interdependent behavior. We hypothesize that this is because for a larger XstallD, the stall current and hence the thermal losses would be lower, which would require a lower Th2tD to cause the same tripping behavior. Due to this interdependency, it would still be difficult to identify both parameters uniquely within the dark blue region.

Finally, we illustrate how thresholding nonlinearity impacts the parameter dependency by contouring VstallD and XstallD. VstallD is the stall voltage of motor D, which we also highlighted in Figure 3.3 and Section 3.2. This Figure 4.3 agrees with our analysis from Section 3.2. Note that we change the voltage trip level here, whereas Figure 3.3 changed the minimum fault voltage. When the stall voltage VstallD is set below the minimum fault voltage of 0.3703 p.u., neither its own value nor that of the stall reactance matters, which leads to the dark red area at the bottom of the contour. Above 0.3703 p.u., the vertical contour lines mean that VstallD does not matter. However, since VstallD is higher than the minimum fault voltage, the motor will stall, so XstallD does impact the simulation result.

14
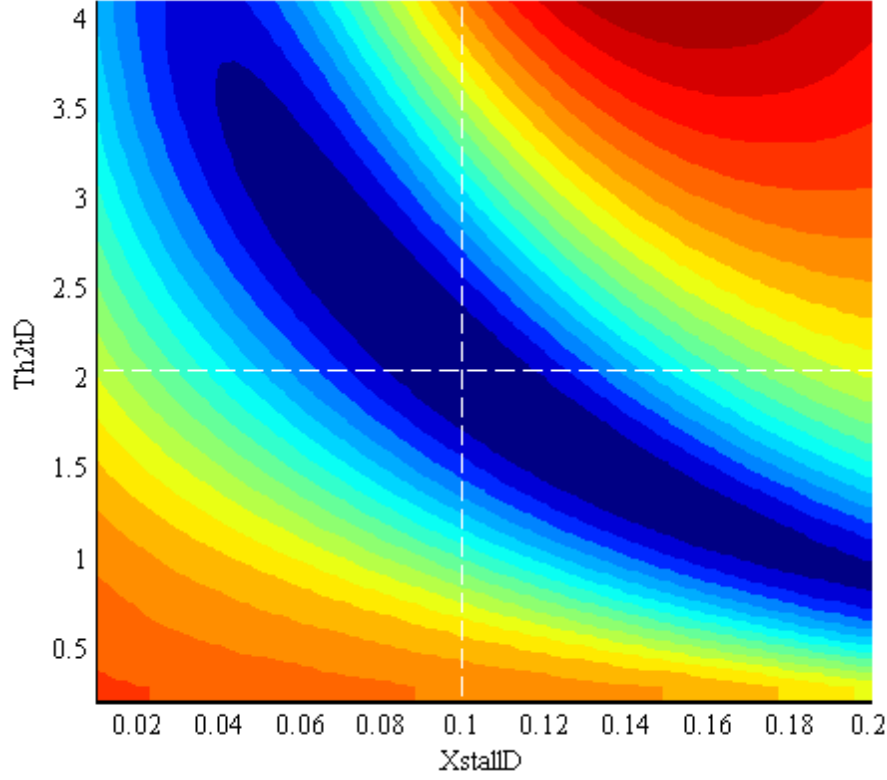
Figure 4.2: Contour of the MSE for two relatively sensitive parameters. XstallD and Th2tD are the stall reactance and the thermal protection trip completion temperature for motor D, respectively.

4.2 SVD-based dependency analysis

If the trajectory sensitivity vectors of several parameters are very similar, then it is possible several combinations of these parameter values will produce the same output response. Hence, the parameter dependency analysis boils down to the problem of finding the parameters of similar trajectory sensitivity. As the length of each $\mathbf{J}_i$ is the total number of output samples, its value T can be very large. To reduce the dimension of feature vectors, we will first perform the singular value decomposition (SVD) [20] on matrix $\mathbf{J}$. To analyze the dependency of parameters with vastly different sensitivities, we first normalize each $\mathbf{J}_i$ to make the parameters comparable. With $T >> N$, the compact singular value decomposition (SVD) of the Jacobian matrix $\mathbf{J}$ is given by:

$$\mathbf{J} = \mathbf{U} \cdot \mathbf{\Sigma} \cdot \mathbf{V}^{\mathrm{T}} \tag{4.1}$$

where the $T \times N$ matrix $\mathbf{U} = [\mathbf{u}_1, \ldots, \mathbf{u}_N]$ consists of the N orthonormal left-singular vectors satisfying $\mathbf{U}^{\mathrm{T}}\mathbf{U} = \mathbf{I}$; and similarly for the right-singular vectors in the $N \times N$ matrix $\mathbf{V} = [\mathbf{v}_1, \ldots, \mathbf{v}_N]$. The diagonal matrix $\mathbf{\Sigma} = \mathrm{diag}\{\sigma_1, \sigma_2, \cdots, \sigma_N\}$ contains the N singular values ordered by $\sigma_1 \geq \sigma_2 \geq \cdots \geq \sigma_N \geq 0$. Clearly, each column of (4.1) can be represented as

15
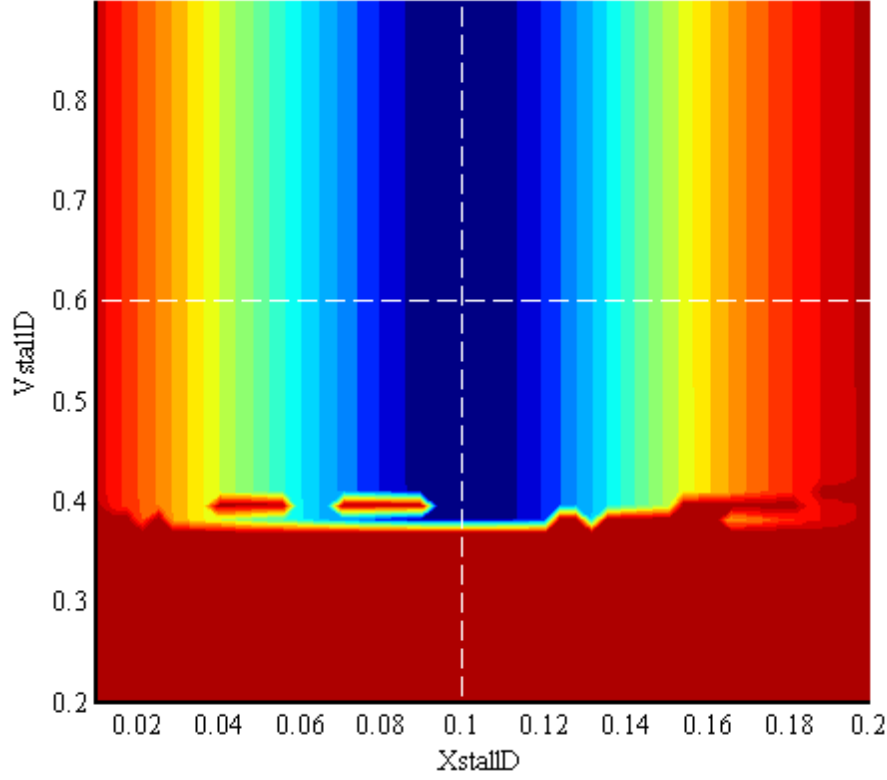
Figure 4.3: Contour of the MSE which highlights the effect of thresholding nonlinearity. XstallD, the stall reactance for motor D, is continuous, but VstallD, the stall voltage of motor D, is discontinuous.

$\mathbf{J}_i = \sum_{n=1}^{N}(\sigma_n v_{n,i})\mathbf{u}_n$, where $v_{n,i}$ is the i-th entry of $\mathbf{v}_n$. Hence, each $\mathbf{u}_n$ can be viewed as a common principle component (PC) of all vectors $\{\mathbf{J}_i\}$, where the scaled vector $\sigma_n \mathbf{v}_n^{\mathsf{T}}$ contains the weights that every $\mathbf{J}_i$ participates in the n-th PC, or the participation factors.

Fig. 4.4 (a) plots all N singular values for the normalized Jacobian matrix. Clearly, the magnitude of σ_n decreases rapidly when $n \leq 20$, implying the first few PCs are much more dominant in forming $\mathbf{J}_i$ compared to the rest. Hence, $\mathbf{J}_i$ can be well approximated using the first $L < N$ PCs, as given by $\mathbf{J}_i \approx \mathbf{J}_i^L := \sum_{n=1}^{L}(\sigma_n v_{n,i})\mathbf{u}_n$. In fact, the approximation error ratio using the first L PCs can be quantified using [20]:

$$\eta_L := \frac{\|\mathbf{J} - \mathbf{J}^L\|_F}{\|\mathbf{J}\|_F} = \frac{\sqrt{\sum_{n=L+1}^{N}\sigma_n^2}}{\sqrt{\sum_{n=1}^{N}\sigma_n^2}} \tag{4.2}$$

where $\|\cdot\|_F$ denotes the matrix Frobenius norm. Fig. 4.4 (b) plots the approximation error ratio value versus the number of PCs L. To achieve $\eta_L < 10\%$ one can select $L = 16$ PCs, while for $\eta_L < 1\%$, $L = 35$ suffices. Hence, we can approximate each $\mathbf{J}_i$ of length T using a much smaller
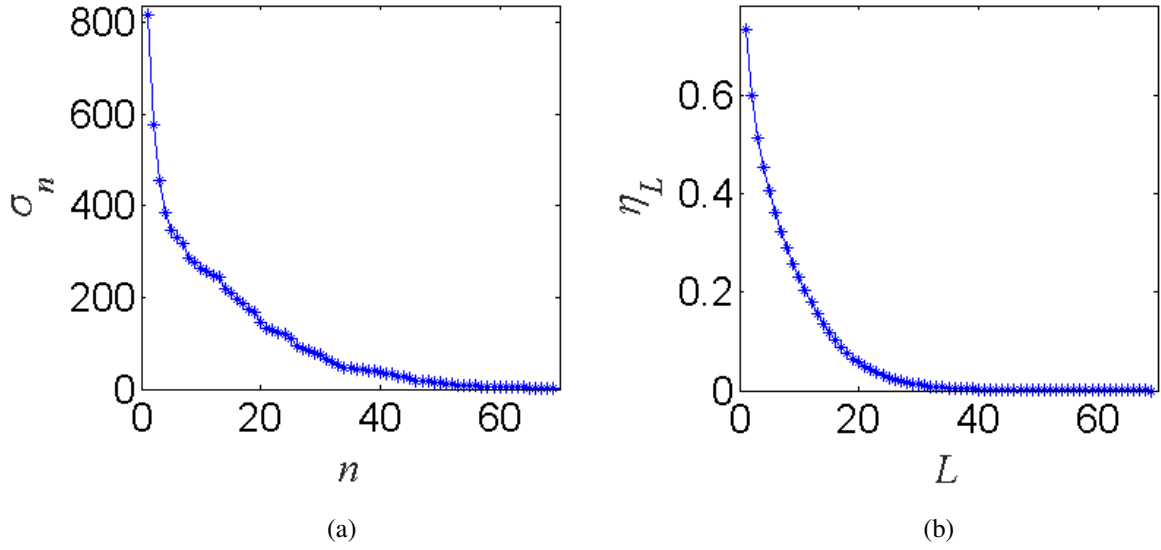
Figure 4.4: For the normalized Jacobian matrix: (a) its singular values σ_n in descending order; (b) the approximation error ratio η_L using the first L PCs. Both are obtained using the PQube dataset #1.

number of PCs with excellent approximation accuracy.

4.3 K-medoids clustering

The K-medoids algorithm [12] is adopted to cluster the N parameters using the trajectory sensitivities $\mathbf{J}_i$ as feature vectors. Given the number of clusters K, K-medoids aims to find the cluster assignment $\{\mathcal{C}_k\}_{k=1}^K$ that minimizes the overall distance between any input vector and the medoid of its assigned cluster. K-medoids is preferred over the classical K-means clustering for its improved robustness to noise and outliers [12]. To this end, define the distance between any two parameters i and j using the Euclidean-norm dissimilarity measure as follows:

$$d_{ij} = \|\mathbf{J}_i - \mathbf{J}_j\|_2. \tag{4.3}$$

The approximate feature vectors $\{\mathbf{J}_i^L\}$ of reduced dimension can be leveraged to facilitate the distance computation in (4.3), which is an effective pre-processing approach in high-dimensional data clustering . In particular, the approximate dissimilarity metric can be defined by:

$$d_{ij} \approx \|\mathbf{J}_i^L - \mathbf{J}_j^L\|_2 = \sqrt{\sum_{n=1}^L \sigma_n^2 (v_{n,i} - v_{n,j})^2}. \tag{4.4}$$

For given distance metric and clustering assignment $\{\mathcal{C}_k\}_{k=1}^K$, the medoid of each cluster k is defined as:

$$c_k := \arg\min_{j \in \mathcal{C}_k} \sum_{i \in \mathcal{C}_k, i \neq j} d_{ij}, \qquad (4.5)$$

which has the minimum summed distance from other parameters within the same cluster. The overall distance minimization problem for K-medoids thus becomes:

$$\min_{\{\mathcal{C}_k\}} \sum_{k=1}^K \sum_{i \in \mathcal{C}_k} d_{ic_k} \qquad (4.6)$$

where c_k is the medoid of $\mathcal{C}_k$ given by (4.5). Albeit non-convex, the optimization problem (4.6) is typically solved by the partitioning around medoids (PAM) algorithm [12].

To evaluate the K-medoids clustering results, one can use the silhouette value [21]. If parameter i is assigned into $\mathcal{C}_k$, its average intra-cluster dissimilarity is defined as:

$$a(i) := \frac{1}{|\mathcal{C}_k| - 1} \sum_{j \in \mathcal{C}_k, j \neq i} d_{ij}, \qquad (4.7)$$

while the definition of inter-cluster dissimilarity is given by:

$$b(i) := \min_{k' \neq k} \frac{1}{|\mathcal{C}_{k'}|} \sum_{j \in \mathcal{C}_{k'}} d_{ij}. \qquad (4.8)$$

The silhouette value of parameter i is defined as:

$$s(i) = \frac{b(i) - a(i)}{\max\{a(i), b(i)\}}, \qquad (4.9)$$

which by definition satisfies $-1 \leq s(i) \leq 1$. The closer $s(i)$ is to 1, the better the cluster assignment for parameter i is. In general, a large average silhouette value over all input parameters (close to 1) indicates that the clustering assignment is of good quality.

Fig. 4.5 (a) plots the average silhouette values for the K-medoids clustering results under different numbers of clusters K. From this figure, we have chosen $K = 10, 20$, and 30 for further investigation, and plotted the average silhouette values of each cluster for these K choices in Figs. 4.5 (b)-(d). When $K = 10$, most of the average cluster silhouette values are quite small, or even negative, indicating that the cluster assignment is poor. However, if K increases to 30, a majority of clusters have just a few elements, or even consist of a single element. Such an assignment prevents us from drawing useful conclusions on the similarity among parameters. Finally, we have selected $K = 20$ as a compromise between silhouette values and preferred cluster size. Some of the example cluster assignments under $K = 20$ are listed in Table 4.1. As expected, quite a few clusters contain the motor parameters of the same property. For example, $\mathcal{C}_{16}$ contains the fraction of motors that obey the second low voltage trip level of motors B and C, {Ftr2B, Ftr2C}. Interestingly, there are parameters that capture completely different load characteristics clustered in a group. For example, XstallD the stall reactance, Th2tD the thermal protection trip completion temperature, and TthD, the thermal time constant for motor D are grouped in $\mathcal{C}_2$. Although they are not directly related, they exhibit strong interdependency as validated in Section 4.5.

18
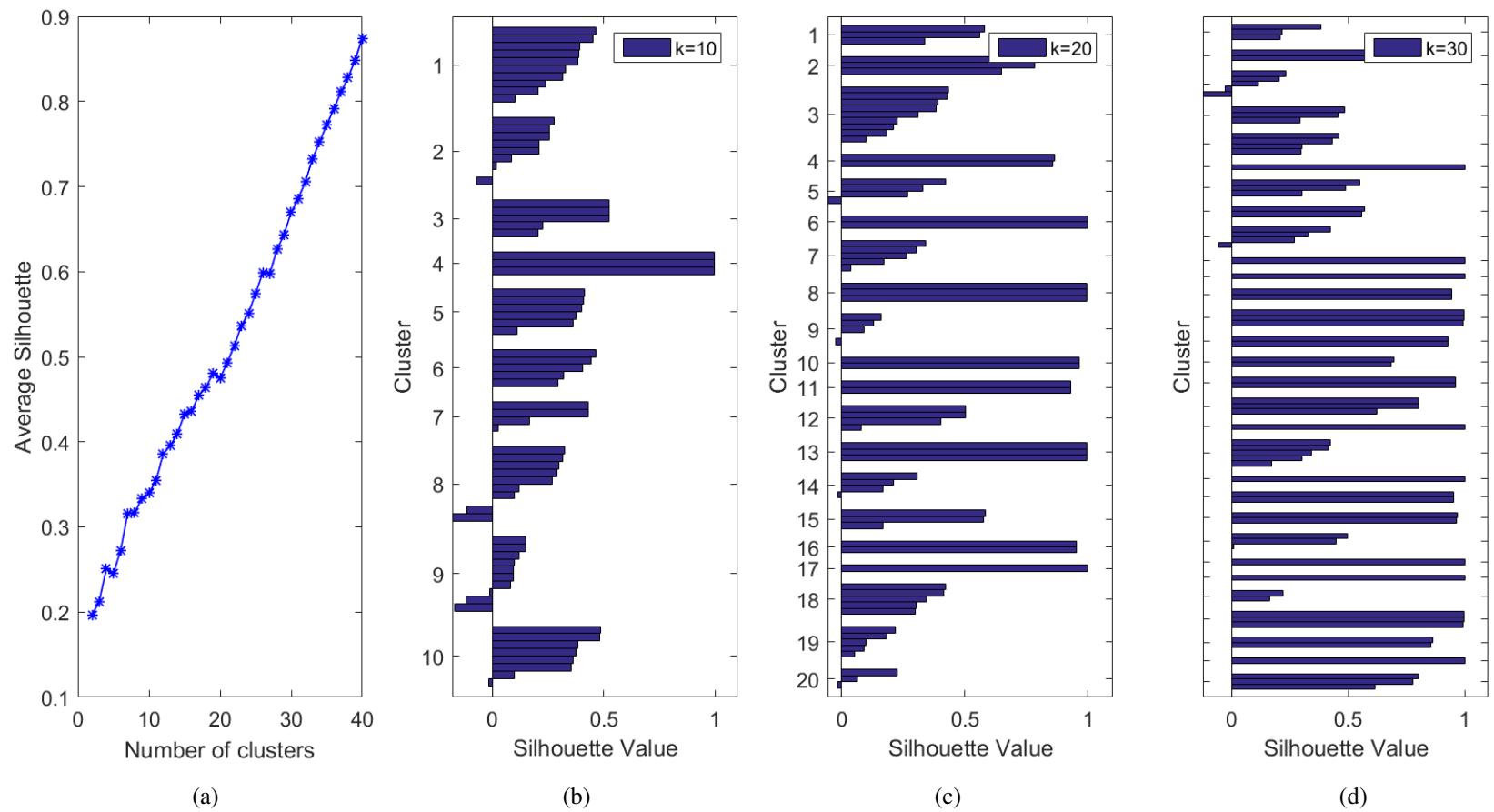
Figure 4.5: (a) The average silhouette values under different numbers of clusters K, and silhouette values of each parameter for (b) $K = 10$; (c) $K = 20$; and (d) $K = 30$.

Table 4.1: Selected K-medoid Clustering Assignments using $K = 20$

Cluster	Parameters
2	XstallD, Th2tD, TthD
4	HA, HC
6	Trc1B, Trc1C
8	Vtr2A, Vtr1B, Vtr1C
10	Ttr2B, Ttr2C
11	Q1c, Q2c
13	Ttr2A, Ttr1B, Ttr1C
16	Ftr2B, Ftr2C

4.4 MDS-based visualization

In addition to the quantitative clustering results, we further employ the multidimensional scaling technique [13] to provide an intuitive visualization of the CMPLDW parameter dependency. MDS aims to map high-dimensional inputs to a lower p-dimensional space while best preserving pairwise dissimilarity of the data. For a given dissimilarity measure $\{d_{ij}\}$ among any parameter pair (i, j), MDS will output a low-dimensional representation $\mathcal{X} := \{\mathbf{x}_i\}_{i=1}^{N}$ of dimension p. Specifically, the dissimilarity can be preserved by solving the following optimization problem:

$$\min_{\mathcal{X}} \sigma\left(\mathcal{X}\right) := \left\{ \frac{\sum_{i,j} \left[\|\mathbf{x}_i - \mathbf{x}_j\|_2 - d_{ij}\right]^2}{\sum_{i,j} \|\mathbf{x}_i - \mathbf{x}_j\|_2} \right\}^{1/2} \tag{4.10}$$

where the defined error objective $\sigma\left(\mathcal{X}\right)$ is known as the *Kruskal Stress* [13]. The smaller $\sigma(\mathcal{X})$ is, the better the MDS mapping is. The minimization problem (4.10) can be solved using a variety of iterative methods, such as the gradient descent or the majorization technique [13]. These iterative algorithms can be initialized based on the SVD results; i.e., using the first p participation factors $\sigma_n \mathbf{v}_n^{\mathsf{T}}$ as the initial guess for entries of $\mathbf{x}_i$.

Fig. 4.6 illustrates the 2-dimensional MDS mapping $\{\mathbf{x}_i\}$ for the CMPLDW model parameters. A reasonably small objective value $\sigma(\mathcal{X}) = 0.21$ has been obtained for this MDS mapping. To better evaluate the MDS results, the K-medoids clustering assignment in Fig. 4.5 (c) under $K = 20$ has been added to each parameter, showing that the clusters are well separated in this 2-dimensional space. In particular, the clusters listed in Table 4.1 can be easily identified in this figure. The MDS results are effective for visualizing the parameter dependency.

4.5 Numerical results

We investigate two of the parameter clusters obtained by the above dependency analysis. Based on Table 4.1, we select the parameters in clusters $\mathcal{C}_2$ and $\mathcal{C}_4$ and compare the similarity of their trajectory sensitivity profiles, as plotted in Fig. 4.7. For the parameters that are within either
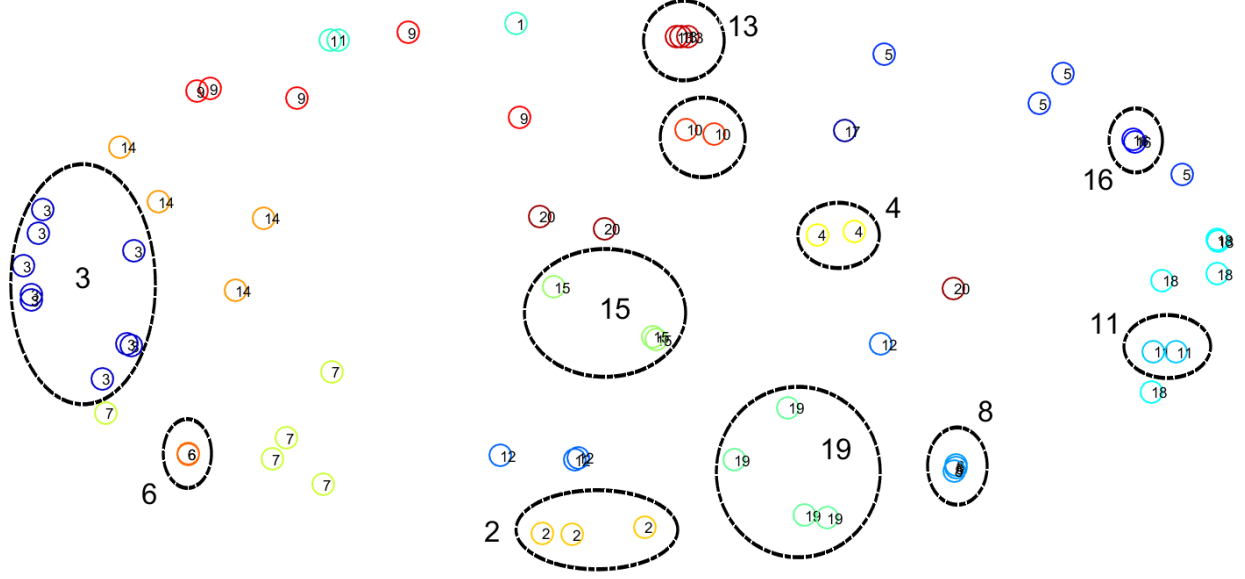
Figure 4.6: MDS result for the $N = 70$ parameters in a 2-dimensional space: each circle represents a parameter, while the larger ellipses correspond to the K-medoids clusters under $K = 20$ in Fig. 4.5 (c).

Table 4.2: Four modified cases of parameter settings.

	XstallD	Th2tD	TthD		HA	HC
Ini. Case	0.1	2.05	30	**Ini. Case**	0.05	0.1
Case 1	0.1	1.7	38	**Case 3**	0.2	0.01
Case 2	0.105	2.4	23.5	**Case 4**	0.01	0.8

cluster, they share an extremely similar trajectory sensitivity pattern. This observation confirms our earlier dependency analysis results.

Furthermore, Table 4.2 lists four modified cases of parameter settings for the CMPLDW model, all of which result in a nearly identical output response as depicted by Fig. 4.8. The dashed vertical line partitions the response to active and reactive power outputs, respectively. This convention is adopted for all the ensuing output response plots. Compared to the initial case, cases 1-4 are produced by varying the values of parameters in either $\mathcal{C}_2$ or $\mathcal{C}_4$. Due to the similar trajectory sensitivity pattern, the effect of changing the value of one parameter could be compensated by that of other parameters in the same cluster, which makes the resultant dynamic responses indistinguishable. For example, in case 1, the thermal time constant TthD is increased from 30 to 38, while the thermal protection trip completion level Th2tD is decreased from 2.05 to 1.7. Still, the dynamic response stays almost the same as the initial case. This reveals the parameter identifiability issue and manifests the necessity of the dependency analysis.
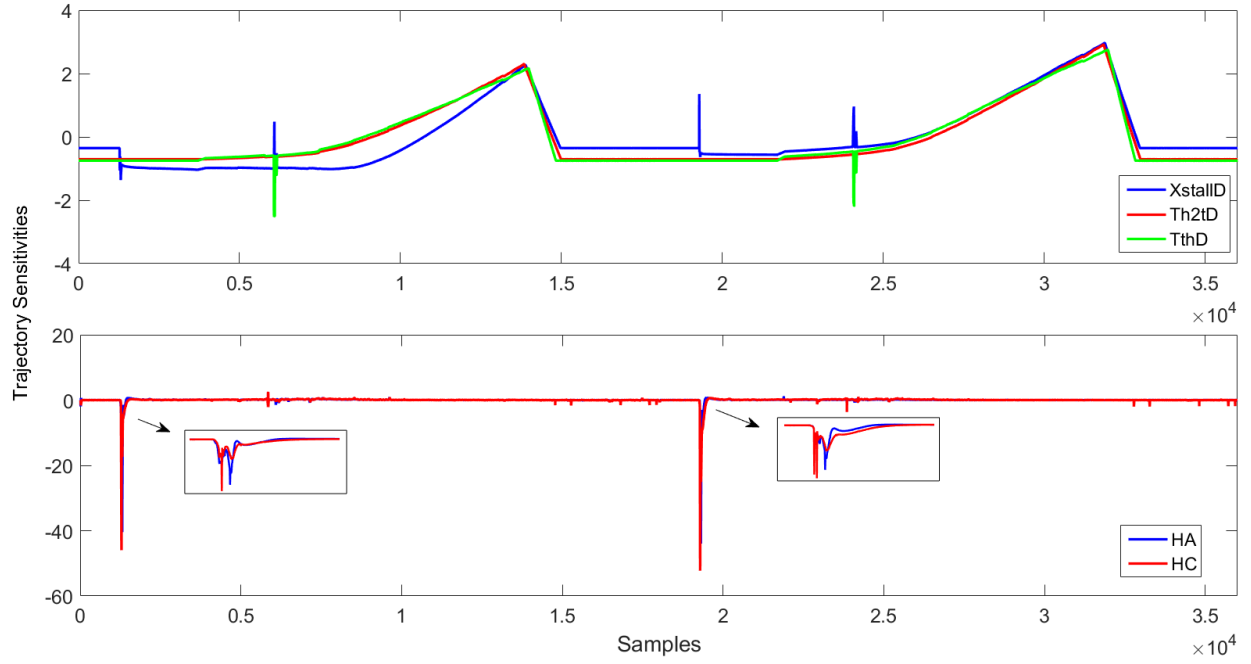
Figure 4.7: Comparison of the normalized trajectory sensitivity for the two parameter clusters in Table 4.1: (top) $\mathcal{C}_2 = \{$XstallD, Th2tD, TthD$\}$, and (bottom) $\mathcal{C}_4 = \{$HA, HC$\}$.
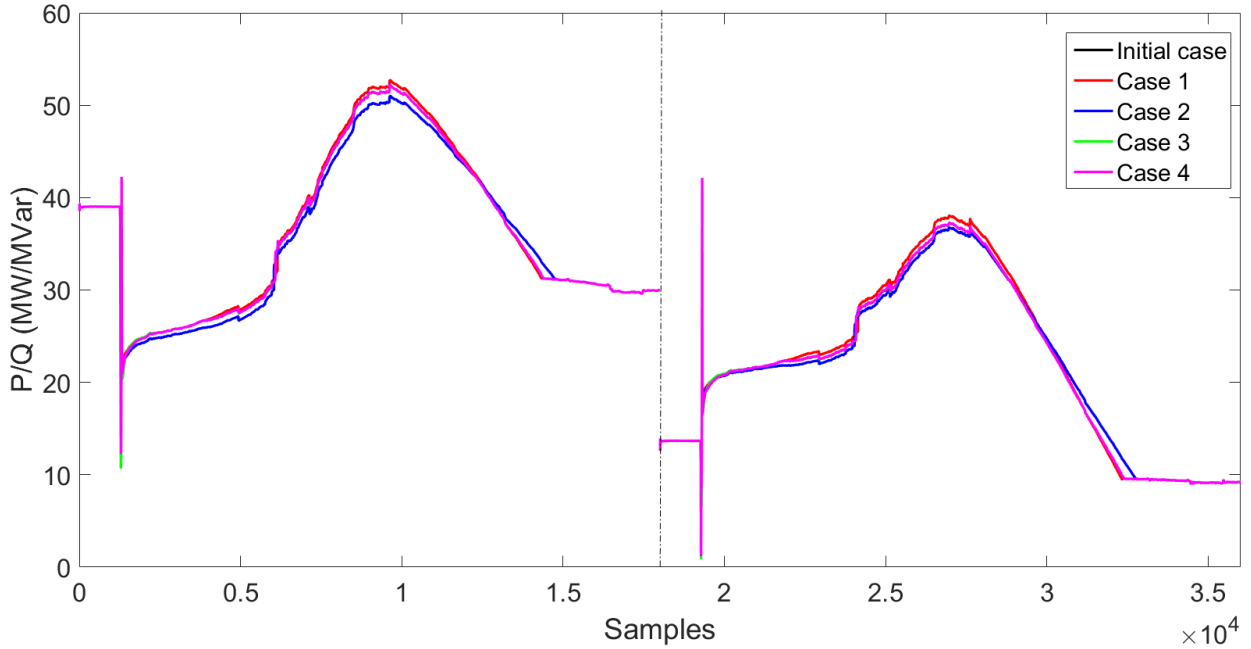
Figure 4.8: The active/reactive power outputs under the four cases of different parameter settings as listed in Table 4.2.

Chapter 5

Effects on Load Modeling

5.1 Parameter estimation using noisy measurements

In [17], we found that the CLOD model, being highly non-linear, also had interdependent parameters. We found that out of the five submodels in CLOD, there were only 2 distinct responses. Specifically, the large motor, small motor, and constant power submodels produced very similar responses to the disturbance. The discharge lighting and PI/QZ submodels produced a second re-
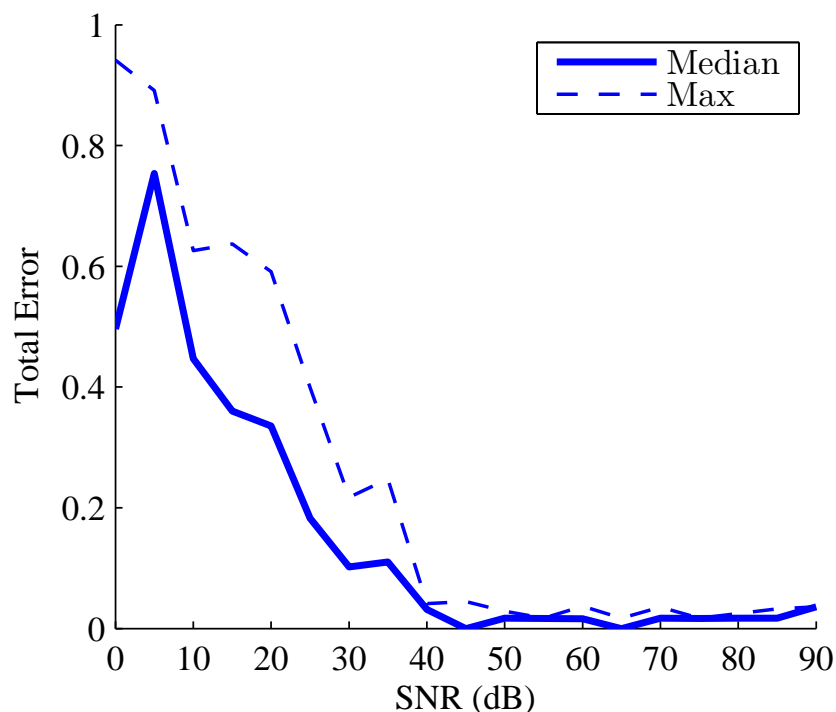
Figure 5.1: The total estimation error as a function of the measurement SNR.

sponse. Thus, the responses have become very insensitive to the parameter values. Conversely, the parameter estimate becomes very sensitive to the measured waveforms, and in particular, noise. Another way to understand this is that the optimization problem outlined in Section 2.3 is very ill-conditioned, in that the cost function is very flat near the optimal solution. In the ideal case, we could still converge to the correct optimal solution, albeit with more iterations.

However, when measurement noise is introduced, the ill-conditioning of the problem means that the correct solution can no longer be attained. In Fig. 5.1, first presented in [17], we showed the total error as a function of the signal to noise ratio (SNR) of the measurements, by adding white Gaussian noise to $\mathbf{y}$, in increments of 5 dB between 0 dB and 90 dB. for each level of noise, 5 realizations of the random noise are tested, and the median and maximum of those 5 trials are shown. We can see that as the SNR drops below 40 dB, the noise causes the error to behave erratically due to the global minimum jumping unpredictably between multiple local minima created by the addition of noise. The reader may notice that the error does not decrease monotonically as SNR increases. This can be attributed to the fact that we average over only 5 realizations of noise, to keep computation time reasonable. The non-monotonicity seen in Fig. 5.5 and Fig. 6.2 is also due to this.

5.2   Impact on model prediction accuracy

In the previous section, we showed how the CLOD model had interdependent parameters, and looked at how this manifests itself in the inability of the parameter estimation to find the correct minimum when the measurements contain noise.

One could argue, however, that another interpretation of the results is that when several parameter estimates all produce similar simulation results, then there is no need to differentiate between those results. In other words, as long as the residual, $\mathbf{y} - \mathbf{f}(\hat{\boldsymbol{\theta}})$ is small, then $\hat{\boldsymbol{\theta}}$ is a good solution. If this is true, then for CLOD we really only needed a model with two degrees of freedom, and the question becomes simply identifying and grouping parameters that behave similarly. However, we will now show that while this will work for the particular fault we used in Section 5.1, we will run into problems when we try to reuse this model in the future to predict responses to other faults. Specifically, we will look at whether the model is able to produce correct transient simulation results for faults at other buses on a system. In the language of machine learning, we wish to see how a model's performance on the training data set translates into performance on the test data set. The system we will use is the 37 bus case from [22], which contains 57 branches, 9 generators, 25 loads, and bus voltages ranging from 69 kV to 345 kV. It is shown in Fig. 5.2. The fault bus, bus 1, is highlighted.

In Fig. 5.3, we show how the accuracy of a model that is derived from a disturbance at one bus impacts the accuracy of simulations performed using the model on the same type of disturbance at other buses. In this figure, there are 127 data points, each one representing one set of load model parameters, $\hat{\boldsymbol{\theta}}_k$, generated from a uniform sampling of possible model parameters. On the horizontal axis, the model residual for a point k is defined as:
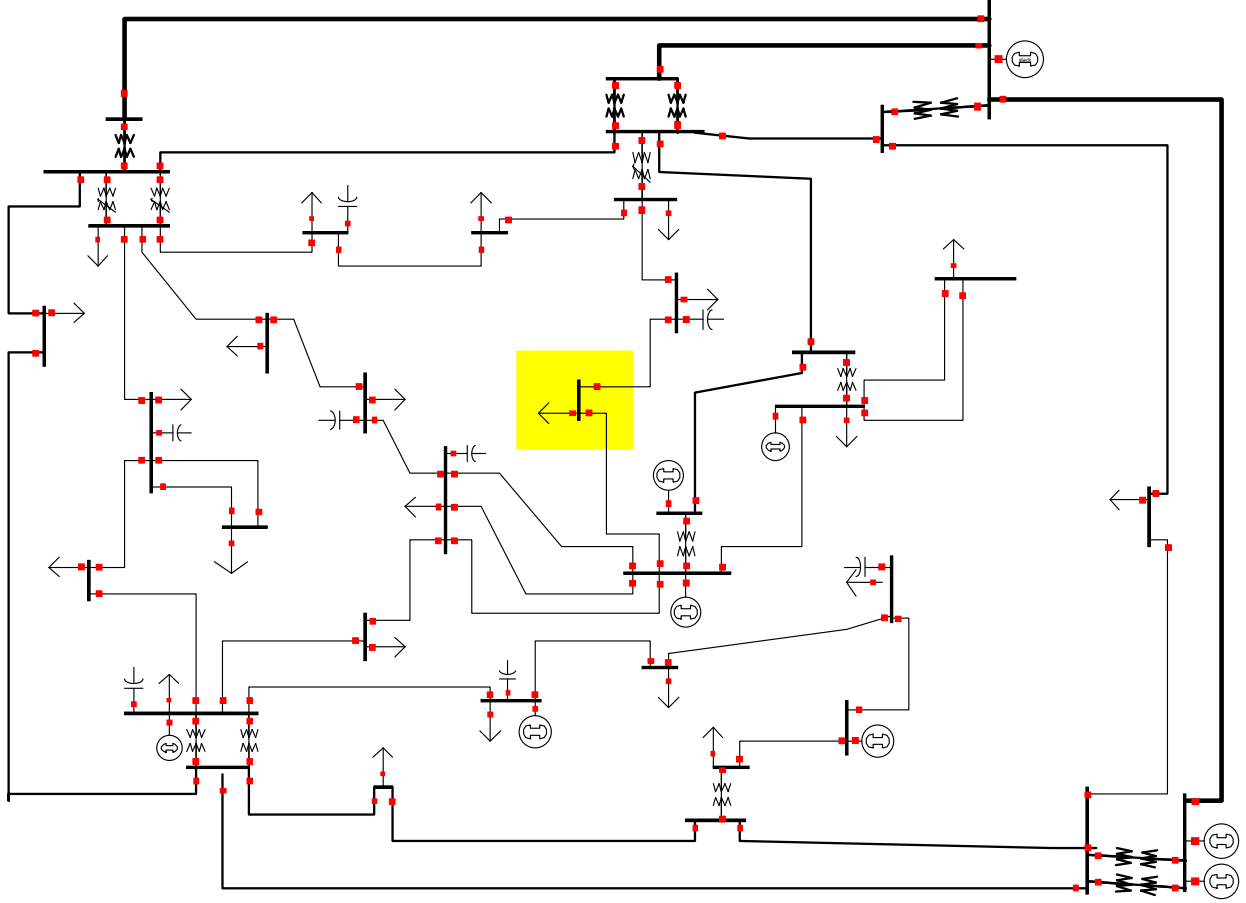
Figure 5.2: 37 bus case from [22] used for validation (fault bus highlighted).

$$\|\mathbf{y}_1 - \mathbf{f}_1(\boldsymbol{\theta}_k)\|_2^2 \tag{5.1}$$

This is the error when the model k is applied to the training fault, with measurements denoted by $\mathbf{y}_1$ and simulation $\mathbf{f}_1$. Note that when we perform parameter estimation based on a fault at bus 1, we try to find $\boldsymbol{\theta}$ to minimize (5.1). On the vertical axis, mean prediction residual for a point k is defined as:

$$\frac{1}{36} \sum_{n=2}^{37} \|\mathbf{y}_n - \mathbf{f}_n(\boldsymbol{\theta}_k)\| \tag{5.2}$$

This is the average error if the model $\boldsymbol{\theta}_k$ were used to predict the results of a disturbance at the other buses ($n \in [2, 37]$). The red line is the line of best fit for the 127 data points. Finally, the shaded area represents the range of the prediction residual, between $\min_{n \in [2,37]} \|\mathbf{y}_n - \mathbf{f}_n(\boldsymbol{\theta}_k)\|$ and $\max_{n \in [2,37]} \|\mathbf{y}_n - \mathbf{f}_n(\boldsymbol{\theta}_k)\|$.
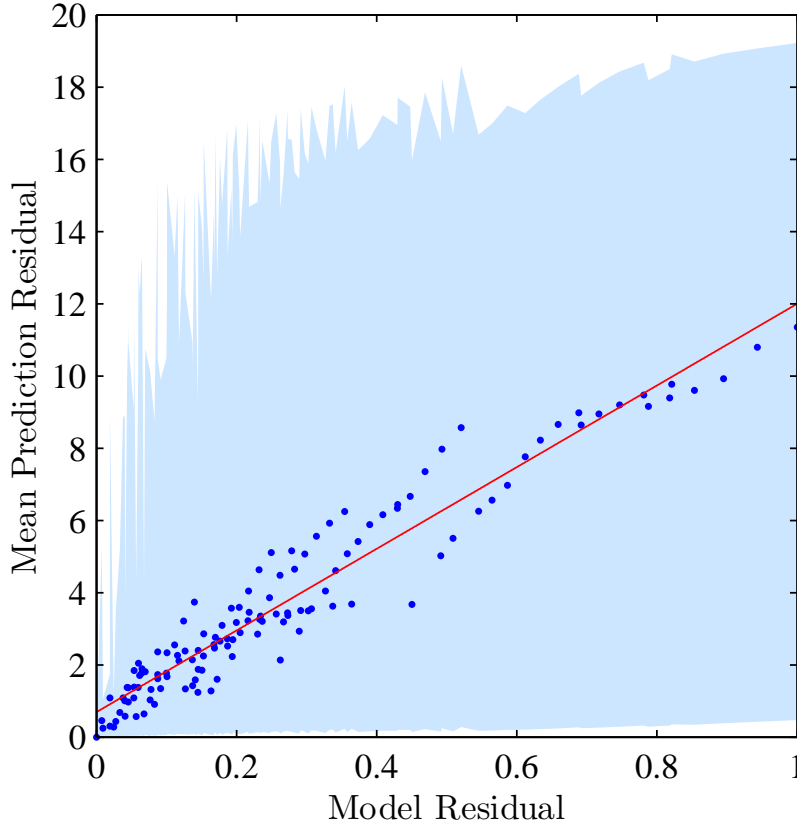
Figure 5.3: The accuracy of a model on the training disturbance is on the X axis. The accuracy of the model on the test disturbances is on the Y axis. Small errors in the derivation of a model from one disturbance leads to large errors when that model is applied to other disturbances.

From the points in Fig. 5.3, we can see that there is a clear correlation between the accuracy of the model derived from bus 1, and the accuracy when it is applied to other buses. Models that produced waveforms that were closest to the measurements $\mathbf{y}$ (i.e. small model residual), could be expected to perform better on average than most other models when applied to other disturbances. However, if we look at the axes, we can see that their scales are very different: the slope of the red line is 11.31, meaning that every unit of error when generating the model results in, on average, 11.31 units of error when predicting future disturbances. Additionally, the shaded region shows that the maximum error has an even worse behavior. By the time our model residual is 0.1, our maximum prediction residual has reached 10, a factor of 100 greater. What this ultimately means is that even if a model performs very well on the training data, its ability to perform reasonably on the test data can not be guaranteed.

We can also see this in the time domain. In Fig. 5.4, we chose a data point in Fig. 5.3 with the fifth lowest model residual, henceforth known as $\widetilde{\theta}$. $\widetilde{\theta}$ had a low mean prediction residual, but a relatively high maximum prediction residual. We then plotted waveforms for faults at three
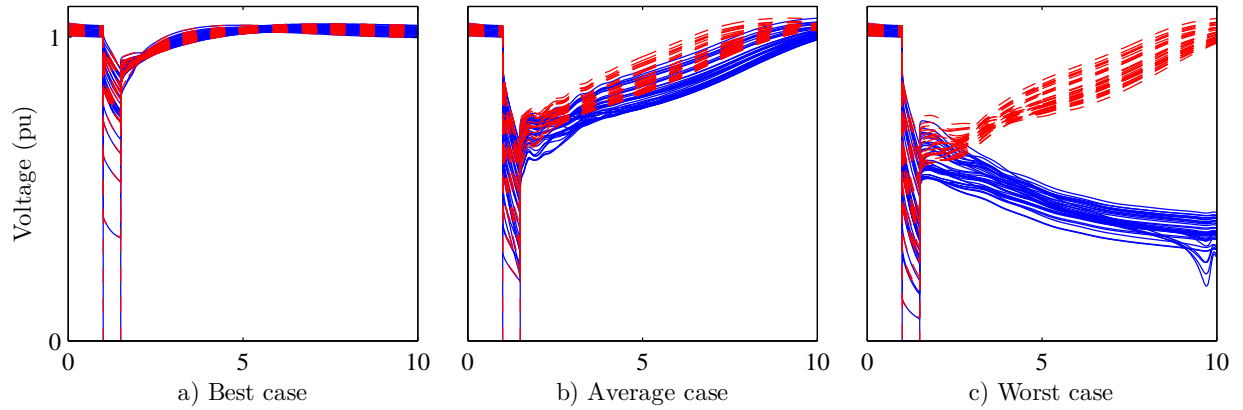
Figure 5.4: Best, average, and worst case for a set of parameters with low model residual. The solid blue lines are the correct transient response at each of the 37 buses, and the dashed red lines are the transient response using incorrect parameters. The horizontal axis is time in seconds.

different buses using the parameters $\widetilde{\theta}$. The average case corresponds with the point for $\widetilde{\theta}$ in Fig. 5.3, the best case with the lower bound in the blue shaded region directly below $\widetilde{\theta}$, and the worst case with the upper bound. Here, we can see that even for parameters that perform very well (the best case and average case are very close), the worst case is still very poor. This means that if we were to use $\widetilde{\theta}$ to estimate a disturbance at another bus, most of the time we will be accurate, but sometimes the simulation will show stability when in fact the system is unstable, or vice-versa. With such uncertainty, researches would find it difficult to draw meaningful conclusions.

5.3 Effect of multiple inputs

In Chapter 4 and Section 5.1, we saw that both the CLOD and CMPLDW models have parameter interdependency, and in Section 5.2, we saw that this decreases our confidence in the CLOD model for predicting the results of other disturbances. In this section, we investigate whether this can be improved by using multiple disturbances, in essence increasing the number of training cases.

In Section 5.2, we saw that a single disturbance is not enough information to determine the correct load model parameters, and an incorrectly chosen set of parameters can have disastrous consequences during future simulations. The reason that noise had such a large effect is that the cost function for one disturbance had multiple local minima. When noise exists in the measurements, the amplitude of these local minima are affected, meaning that the global minimum jumps unpredictably between these minima. In essence, these local minima are all acceptable solutions to the parameter estimation problem for that one disturbance, though only one is the correct model. We can use multiple disturbances to find the local minimum that is common among them.

To implement what was just described, however, is intractable. In order to do this, we would require a list of all the local minima for disturbance 1, and another list for disturbance 2, which we could then compare to find the overlapping minima. For such a non-linear optimization problem,
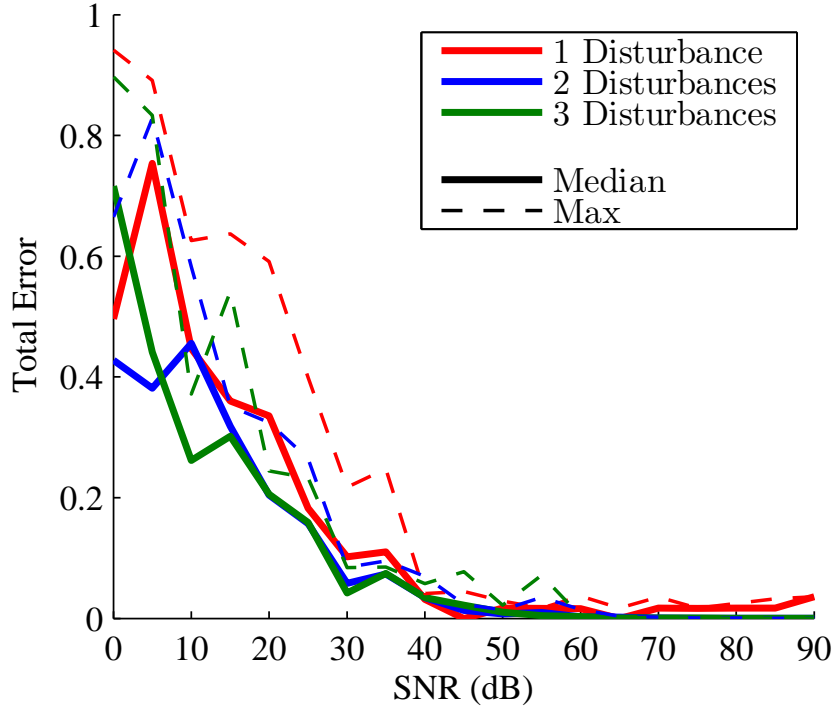
Figure 5.5: Error versus noise for three LSQ estimators: one using a single disturbance, one using two disturbances, and one using three disturbances.

it is computationally intractable to enumerate all the local minima, and we would have no way of determining when we had covered all of them. Instead, we define a list of disturbance buses $\mathcal{B}$, and modify (2.2) to accommodate multiple disturbances:

$$\hat{\boldsymbol{\theta}} = \arg\min_{\boldsymbol{\theta}} \frac{1}{2} \sum_{n \in \mathcal{B}} \|\mathbf{y}_n - \mathbf{f}_n(\boldsymbol{\theta})\|_2^2 \tag{5.3}$$

In Fig. 5.5, we see the result of using two disturbances and three disturbances. We can see that multiple disturbances decrease the maximum error (the dashed line) somewhat, but not significantly. Also, the median error is also only marginally better. Clearly, using multiple disturbances will not allow us to reduce the effects of interdependency to any meaningful extent. In Section 6.1, we look at a second method.

Chapter 6

Improved Parameter Estimation

In this chapter, two improved parameter estimation approaches are proposed. Both methods use *a priori* information to reduce the impact of parameter interdependency.

6.1 Maximum *a posteriori* estimator

In this section, we use a probabilistic maximum a posteriori (MAP) estimator to improve the robustness of the model to measurement noise, and hopefully decrease the negative impact from noise that we saw in Fig. 5.1. A MAP estimator uses prior knowledge of the values that $\boldsymbol{p}$ is most likely to take, in order to eliminate outliers. The source of this knowledge would come from the experiences of system operators.

6.1.1 Formulation

The MAP estimator for a continuous random variable is defined in [23] as:

$$\hat{\boldsymbol{\theta}} = \arg\max_{\boldsymbol{\theta}} \left\{ h_{\Theta|Y}(\boldsymbol{\theta}|\mathbf{y}) \right\} \tag{6.1}$$

Using Bayes' theorem, this can be rewritten:

$$\hat{\boldsymbol{\theta}} = \arg\max_{\boldsymbol{\theta}} \left\{ g_Y(\mathbf{y}|\boldsymbol{\theta}) g_\Theta(\boldsymbol{\theta}) \right\} \tag{6.2}$$

where g_Y is the likelihood function and g_Θ is the prior. The likelihood function captures the information provided by the measurements, and the prior captures the *a priori* knowledge we have of the parameters.

The likelihood function is defined as follows:

$$g_Y(\mathbf{y}|\boldsymbol{\theta}) = \prod_{t=1}^{T} f_Y \left(\frac{\mathbf{y}[t] - \mathbf{f}(\boldsymbol{\theta})[t]}{\sigma_Y} \right)$$

$$\prod_{t=1}^{T} f_Y \left(\hat{\mathbf{y}}[t] \right) \tag{6.3}$$

where f_Y is a chosen probability density function (PDF), σ_Y is a predetermined constant, t is time, and $\hat{\mathbf{y}}$ is the standardized values of $\mathbf{y}$. For this definition of g_Y to be valid, we must assume that values in $\mathbf{y}$ are mutually independent of each other. While this is almost certainly not true, we do not have sufficient information to allow us to calculate the joint probability density function for measurements that are not independent. Thus, we make this simplifying assumption.

The prior is obtained by using experience to make an educated guess of what the parameters should be, $\boldsymbol{\mu_\theta} = \begin{bmatrix} \mu_{\theta(1)} & \cdots & \mu_{\theta(N)} \end{bmatrix}$, as well as their confidence, which could be translated into a standard deviation $\boldsymbol{\sigma_\theta} = \begin{bmatrix} \sigma_{\theta(1)} & \cdots & \sigma_{\theta(N)} \end{bmatrix}$. g_Θ. g_Θ could then be calculated as:

$$
\begin{aligned}
g_\Theta(\boldsymbol{\theta}) &= \prod_{n=1}^{N} f_\Theta \left(\frac{\theta(n) - \mu_{\theta(n)}}{\sigma_{\theta(n)}} \right) \\
&= \prod_{n=1}^{N} f_\Theta \left(\hat{\theta}(n) \right)
\end{aligned}
\tag{6.4}
$$

Again, similar to the case for $g_Y(\mathbf{y}|\boldsymbol{\theta})$, (6.4) is only valid if the parameters are mutually independent. In this case, we know for certain that they are not, because the sum of the parameters must equal 100%. However, there currently exists very little literature on random variables with a constant sum. Thus, we again make the simplifying assumption of independence.

6.1.2 Implementation

The next step is to choose PDFs for f_Y and f_Θ. Based on preliminary testing, we have found that a normal distribution is a good choice for f_Y and a Laplace distribution is a good choice for f_Θ.

The reason why a normal distribution—an extremely common PDF—is unsuitable for f_Y is because of the interaction of g_Y and g_Θ. In (6.2), we multiply the two PDFs together. Thus, when we perform the optimization, what is important is not the values g_Y and g_Θ at an iteration, but rather the relative benefit to the objective function of an improvement in $\boldsymbol{v}$ or $\boldsymbol{p}$. In other words, an improvement of g_Y or g_Θ from $1e{-}3$ to $1e{-}2$ has a greater impact than from 0.1 to 0.2. In Fig. 6.1 we show a standard normal distribution. If we zoom in on the tail of the distribution, we can see that it decays increasingly rapidly at higher numbers of standard deviations from the mean. What this means is that for a unit step at x toward the mean, the relative increase of $f(x)$ is higher for larger values of $|x|$.

When applied to our load model MAP estimator, for f_Θ, it is reasonable for us to use a normal distribution, because we wish to severely penalize the objective function when p is far from $\mu_{\boldsymbol{p}}$. However, in the case of f_Y, this is undesirable. In the case when measurement noise is very high or the measurements are corrupted, we wish to disregard the measurements. However, in this situation $\hat{\mathbf{y}}[t]$ will be large, so we are evaluating f_Y very far from the mean, meaning that the objective function is penalized heavily for following the prior instead of the measurements. On the other hand, when we have measurements with low noise, we should trust the measurements more instead of following the operator's guess. However, in this situation we are evaluating f_Y very close to the mean, where the shallow slope of f_Y results in the prior, f_Θ, dominating.
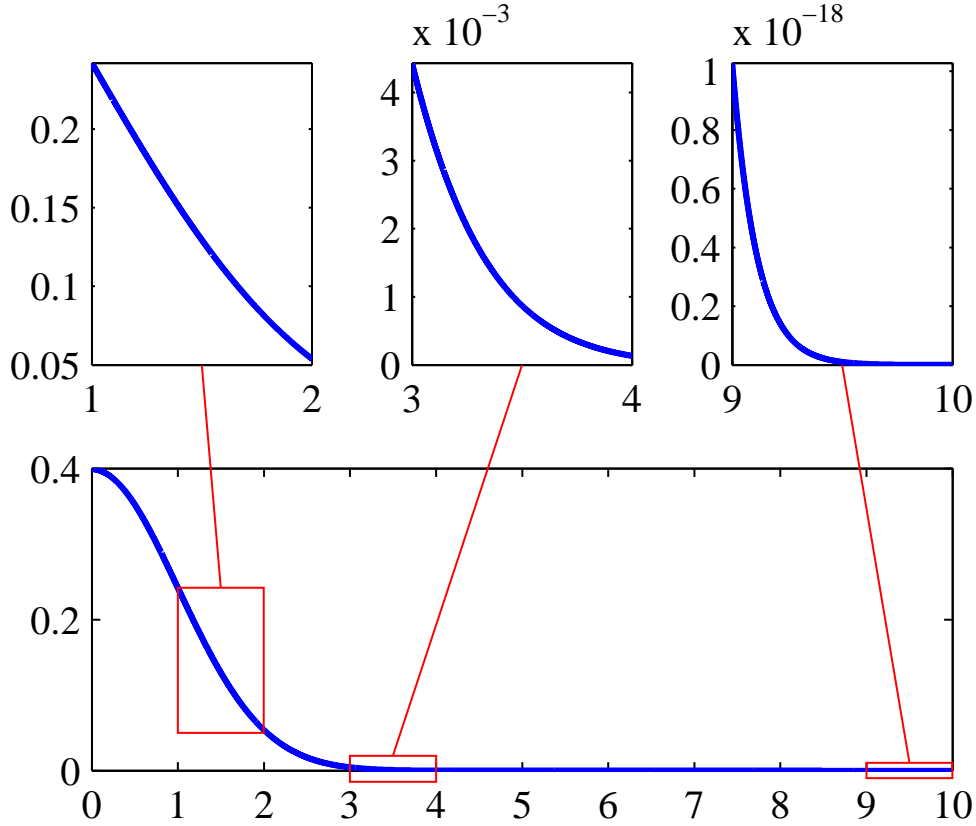
Figure 6.1: The tail of a standard normal distribution decays increasingly rapidly.

The final implementation issue is the assigning of values to $\sigma_\mathbf{y}$ and $\sigma_{\boldsymbol{\theta}}$. While the selection of the appropriate distributions above now allows f_Y to dominate over f_Θ when noise is low, the relative values of $\sigma_\mathbf{y}$ and $\sigma_{\boldsymbol{\theta}}$ will decide how much f_Y dominates. Through empirical testing, we found that setting $\sigma_\mathbf{y} = 0.05$ and $\sigma_{\boldsymbol{\theta}} = 20$ works well.

6.1.3   Results

In Fig. 6.2, we show the estimation error versus SNR for two different sets of $\mu_{\boldsymbol{\theta}}$. The red lines show the case where $\mu_{\boldsymbol{\theta}}$ is set to be equal to the synthetic value; this is a validation scenario with a perfect guess. The blue lines show the case where we have no prior knowledge of $\mu_{\boldsymbol{\theta}}$, so we set $\mu_{\boldsymbol{\theta}} = \begin{bmatrix} 0.2 & 0.2 & 0.2 & 0.2 & 0.2 \end{bmatrix}$. The horizontal black line is the error of this prior (the error for the prior $\mu_{\boldsymbol{\theta}}$ is the synthetic value is zero). From Fig. 6.2, we can see that in low noise scenarios, the choice of prior has little effect on the parameter estimation, and the parameter estimate is comparably accurate for both. This is thanks to our choice of the Laplace distribution for f_Y. In high noise situations, the prior keeps the error from increasing dramatically as we saw in Fig. 5.1.
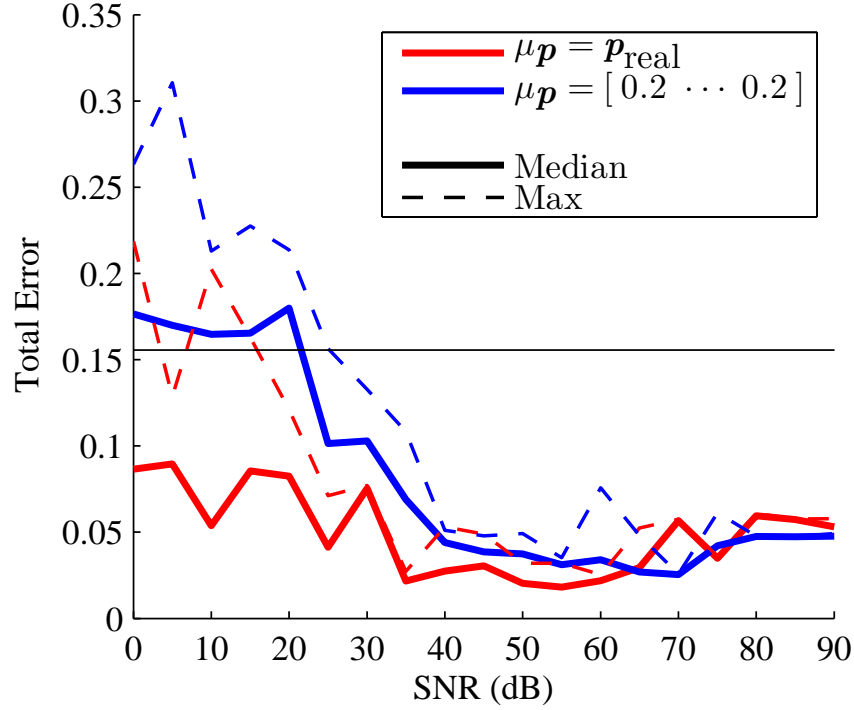
Figure 6.2: Error versus noise for two MAP estimators with different $\mu_{\boldsymbol{\theta}}$.

6.2 Euclidean-norm regularized estimator

6.2.1 Formulation

A high level of dependency among load model parameters reveals the issue of parameter identifiability, which will lead to ill-conditioning of the original NLS estimation problem in (2.1). To tackle this issue, we propose to regularize the NLS objective by incorporating known *a priori* parameter values $\boldsymbol{\theta}_c$, as given by:

$$\min_{\boldsymbol{\theta}} \frac{1}{2}\|\mathbf{y} - \mathbf{f}(\boldsymbol{\theta})\|_2^2 + \frac{\mu}{2}\|\boldsymbol{\Gamma}\left(\boldsymbol{\theta} - \boldsymbol{\theta}_c\right)\|_2^2 \tag{6.5}$$

where $\boldsymbol{\Gamma}$ is a diagonal matrix of all positive values, and the coefficient $\mu > 0$ will be chosen to balance the NLS fitting error and the regularization term. *A priori* parameter setting $\boldsymbol{\theta}_c$ can be obtained either based on load surveys or from historic disturbance data. The regularization term in (6.5) prevents the estimated $\boldsymbol{\theta}$ from changing significantly from the *a priori* $\boldsymbol{\theta}_c$, while minimizing the mismatch between the modeled and measurement output data.

Interestingly, the regularized objective in (6.5) still admits an NLS form if we augment the original measurement function with the following:

$$\min_{\boldsymbol{\theta}} \frac{1}{2}\|\mathbf{y}' - \mathbf{f}'(\boldsymbol{\theta})\|_2^2 := \min_{\boldsymbol{\theta}} \frac{1}{2}\left\|\begin{bmatrix} \mathbf{y} \\ \sqrt{\mu}\boldsymbol{\Gamma}\boldsymbol{\theta}_c \end{bmatrix} - \begin{bmatrix} \mathbf{f}(\boldsymbol{\theta}) \\ \sqrt{\mu}\boldsymbol{\Gamma}\boldsymbol{\theta} \end{bmatrix}\right\|_2^2. \tag{6.6}$$

For this augmented system, the residual error term becomes $\mathbf{r}' := \mathbf{y}' - \mathbf{f}'(\boldsymbol{\theta})$, with the corresponding Jacobian $\mathbf{J_{f'}} = \begin{bmatrix} \mathbf{J}^T & \sqrt{\mu}\boldsymbol{\Gamma}^T \end{bmatrix}^T$. The reformulation in (6.6) suggests solving the regularized NLS problem using the classical L-M algorithm, which iteratively updates $\boldsymbol{\theta}$ as follows:

$$\Delta\boldsymbol{\theta} = -\left(\mathbf{J_{f'}^T J_{f'}} + \lambda\mathbf{D}\right)^{-1} \mathbf{J_{f'}^T r'} \tag{6.7}$$
$$= -\left(\mathbf{J^T J} + \mu\boldsymbol{\Gamma}^T\boldsymbol{\Gamma} + \lambda\mathbf{D}\right)^{-1} \left[\mathbf{J^T r} + \mu\boldsymbol{\Gamma}^T\boldsymbol{\Gamma}\left(\boldsymbol{\theta}_c - \boldsymbol{\theta}\right)\right]$$

where $\mathbf{D}$ is a positive diagonal matrix and λ is the damping coefficient chosen by the algorithm. Matrix $\mathbf{D}$ is usually set to be the identity matrix $\mathbf{I}$ or the diagonal part of $(\mathbf{J}_{\mathbf{f'}}^T \mathbf{J_{f'}})$, in order to improve the conditioning of the inverse operation. As for the damping coefficient, at large λ the update (6.7) would follow the gradient direction $\mathbf{J}_{\mathbf{f'}}^T \mathbf{r}'$, which would guarantee an objective cost reduction. As λ diminishes, it becomes the Gauss-Newton update which can converge geometrically nearby the solution. Thus, typically the value of λ is adaptively adjusted to ensure both the decrease in the objective (6.5) and a satisfactory convergence rate [24].

6.2.2 Implementation

As shown in (6.7), the regularization term can improve the conditioning of the effective Jacobian $\mathbf{J_{f'}}$ and thus benefit the convergence of the L-M algorithm. However, the regularization matrix and coefficient need to be carefully chosen to minimally affect the NLS data fitting mismatch error in (6.5). For example, if μ is too large, the regularization term will dominate the overall objective of (6.5). The resultant estimate would be extremely close to $\boldsymbol{\theta}_c$, and may not effectively diminish the NLS fitting error. We can gradually increase the value of μ from zero until both reasonable estimated parameter values and satisfactory data fitting performance are achieved. As for matrix $\boldsymbol{\Gamma}$, its diagonals determine the penalty on the deviation between each parameter estimation and its *a priori* value. A simple approach is to scale the diagonals of $\boldsymbol{\Gamma}$ to be inversely proportional to the absolute value of the entries of $\boldsymbol{\theta}_c$. One can also incorporate additional information of the variability of parameter values to set the diagonals of $\boldsymbol{\Gamma}$. As suggested by a recent NERC report [11], several motor parameters, such as the loading factor LFmX, synchronous reactance LsX, and transient reactance LpX, can be accurately determined by laboratory tests with small variability in field studies. Accordingly, the corresponding diagonal entries in $\boldsymbol{\Gamma}$ for these parameters can be set to a very large value. On the other hand, some parameters could vary significantly depending on the season, study area, or fault type, including the load component fraction FmX parameters. Smaller values in their corresponding diagonal entries of $\boldsymbol{\Gamma}$ will encourage those parameters to be estimated using more reliable field measurement data, as compared to outdated load surveys.

6.2.3 Results

Numerical tests have been performed to validate the dependency among the WECC CMPLDW parameters, and the effectiveness of the proposed regularized-NLS scheme. The real disturbance measurements collected in PQube datasets #1 or #2 are used. The PowerWorld transient analysis package is employed to simulate the WECC CMPLDW response for a given fault voltage input.

Table 6.1: Selected parameters with actual and estimated values by the NLS and regularized (R-)NLS methods, both performed using the synthetic data with (w/) and without (w/o) noise.

Parameter	Xxf	Pfrq	LFmA	Vrc2A	RsC
Actual value	0.01	-1.3	0.8	0.8	0.01
NLS w/o noise	0.0724	-62.435	0.5828	0.6553	0.4912
R-NLS w/o noise	0.0201	-1.1179	0.6832	0.6468	0.0079
NLS w/ noise	0.0860	109.208	0.3822	0.6441	1.5e-5
R-NLS w/ noise	0.0206	-0.8239	0.6926	0.6487	0.0133

We validate the proposed parameter estimation scheme using both synthetic and real measurement data. To improve the NLS computation efficiency, we have excluded around half of the parameters with (almost) zero trajectory sensitivity from being estimated. Values for these insensitive parameters are fixed at their nominal ones as listed in Table 2.1. The *a priori* parameter setting θ_c used for solving (6.5) is taken from Table 2.1 as well. To select the regularization coefficient μ, its value increases from 0.01 by a factor of 2 until satisfactory fitting results are achieved. As for the diagonal weighting matrix Γ, we use the inverse magnitude of the *a priori* parameter values as its diagonal entries. In addition, for the motor internal parameters of small variability in field studies [11], their corresponding diagonal entries in Γ will be multiplied by a factor of 50.

Using the input voltage from PQube dataset #1, we first generate the modeled active/reactive power outputs with the values of selected parameters changed from nominal ones, as listed in Table 6.1. The noise-free synthetic measurements and the data fitting results using both NLS and regularized NLS methods are plotted in Fig. 6.3. To test the robustness of the two methods to measurement noise, we also add white Gaussian noise to the measurements, as shown in Fig. 6.4 along with the data fitting results. For both noise-free and noisy tests, Figs. 6.3 and 6.4 illustrate that the data fitting error performance for both methods is comparable, with the regularized NLS slightly outperforming the other. Nonetheless, Table 6.1 demonstrates that the regularized NLS achieves much more accurate parameter estimates and better robustness to additive noise, as compared to the original NLS method. For example, the NLS method exhibits "evaporation effects" [24] for parameter Pfrq, the active power frequency dependency factor. Its estimated value -62.4350 under the noise-free setting goes far beyond the nominal range for this parameter. Furthermore, the NLS estimates could be strongly affected by the synthetic measurement noise, as shown for parameters Pfrq and RsC. Under measurement noise, the L-M update could take extremely large steps under the original NLS objective. On the other hand, the regularized NLS estimates not only match well with the actual parameter values, but also show high consistency between the noise-free and noisy scenarios. It is worth noting that although neither method is able to exactly achieve the actual parameter values, the fitting results in the output response are shown to be acceptable. This observation is explained by the issue of parameter identifiability in the CMPLDW model.

We have also validated the performance of the proposed regularized NLS method using the PQube datasets. Fig. 6.5 plots the measured power output data of PQube dataset #2, along with the results attained by the two methods. Although both methods show competitive performance in terms of fitting the output data, the NLS method leads to unreasonable parameter estimate values

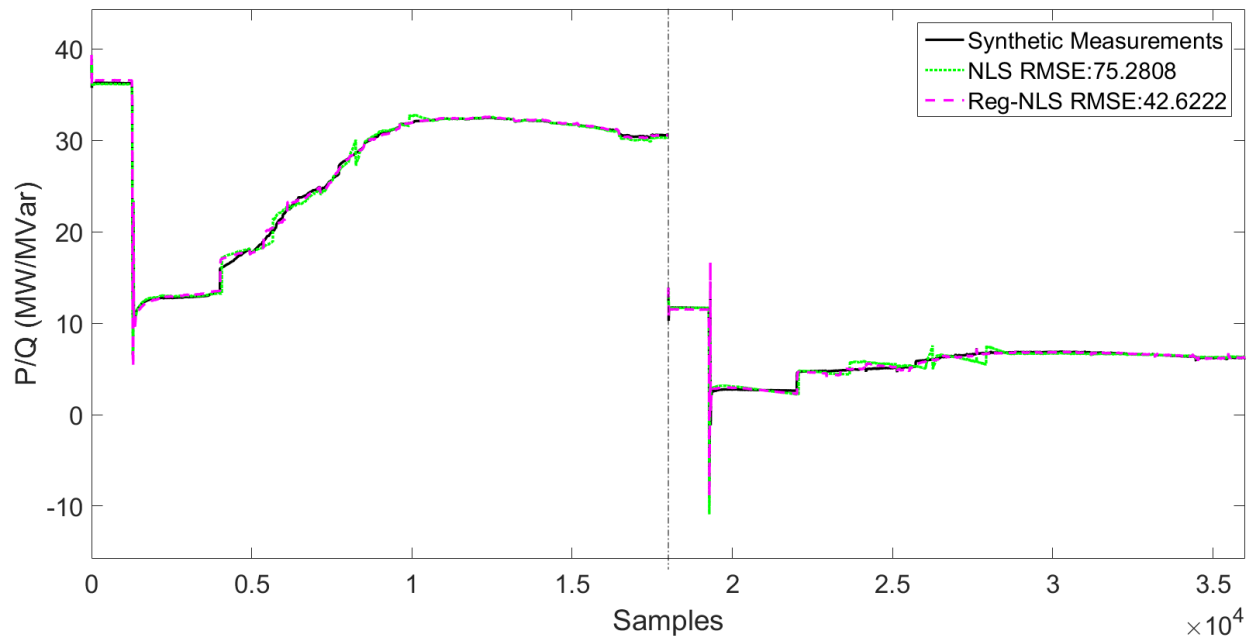Figure 6.3: Noise-free synthetic data and the fitting results attained by the NLS and regularized NLS methods.
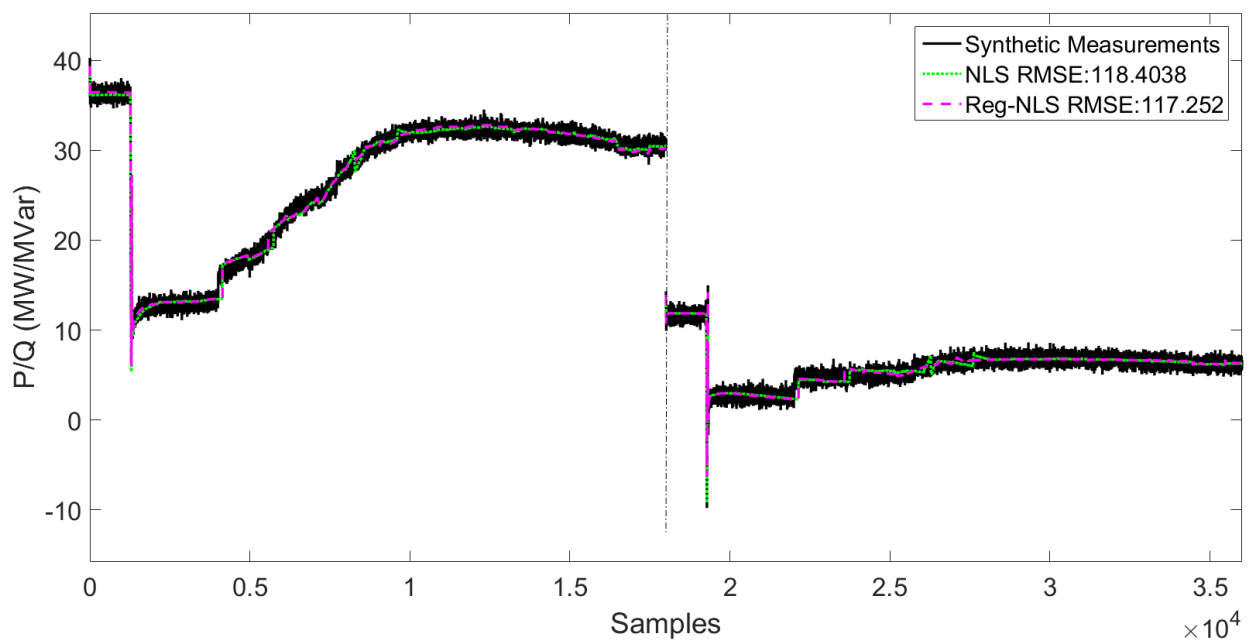

Figure 6.4: Noisy synthetic data and the fitting results attained by the NLS and regularized NLS methods.

as listed in Table 6.2, especially for Pfrq. In some real datasets, the measurement data lacks good quality. This is the case for PQube dataset #1 with several irregular peaks. We first pre-process
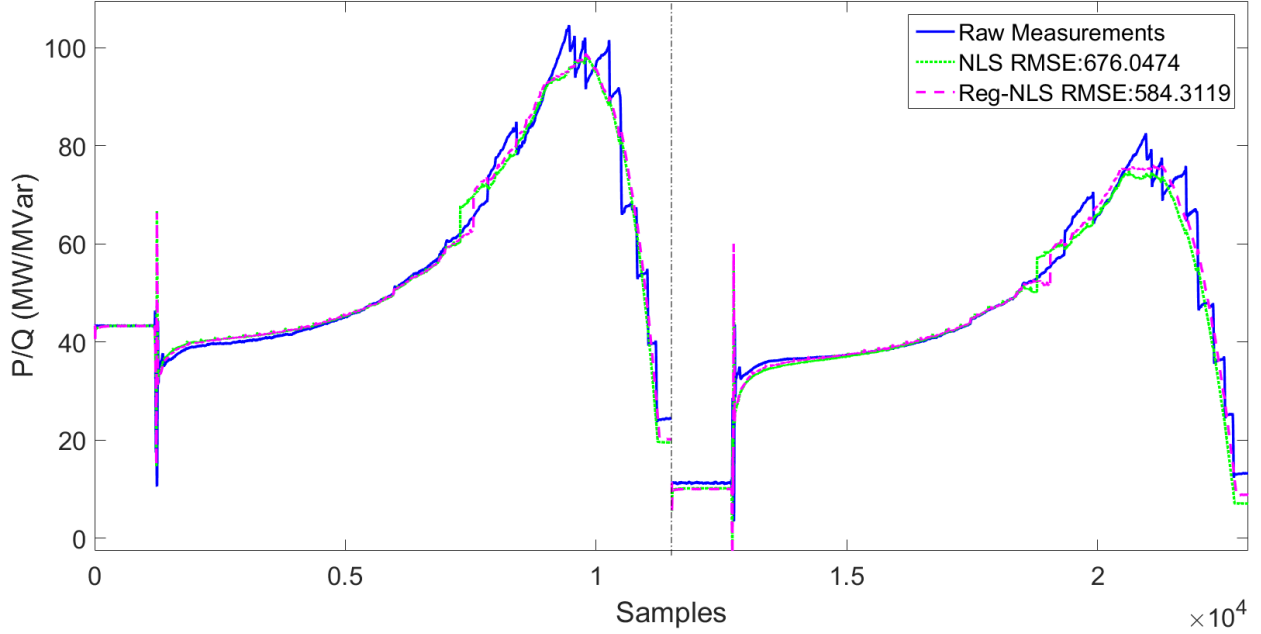
Figure 6.5: PQube dataset #2 and the fitting results attained by the NLS and regularized NLS methods.

Table 6.2: Selected parameter estimates attained by the NLS and regularized NLS methods using PQube dataset #2.

Parameter	Fb	Pfrq	Qfrq	HC	VrstD
NLS	0.1069	-119.04	0.7505	0.2591	1.6219
Reg-NLS	0.4500	-1.2906	-1.0071	0.1005	0.7089

this dataset by smoothing out these peaks. Fig. 6.6 plots the raw output data and its smoothed version, and the latter is used for parameter estimation. Clearly, the proposed regularized NLS method significantly outperforms the original NLS one, in terms of fitting the smoothed and even the raw measurements. Similar comparisons on the estimated parameter values as in Table 6.2 have been observed for PQube dataset #1. By incorporating the *a priori* parameter information, the regularized NLS method has been validated to be of higher accuracy and more robust to noise compared to the original NLS method.
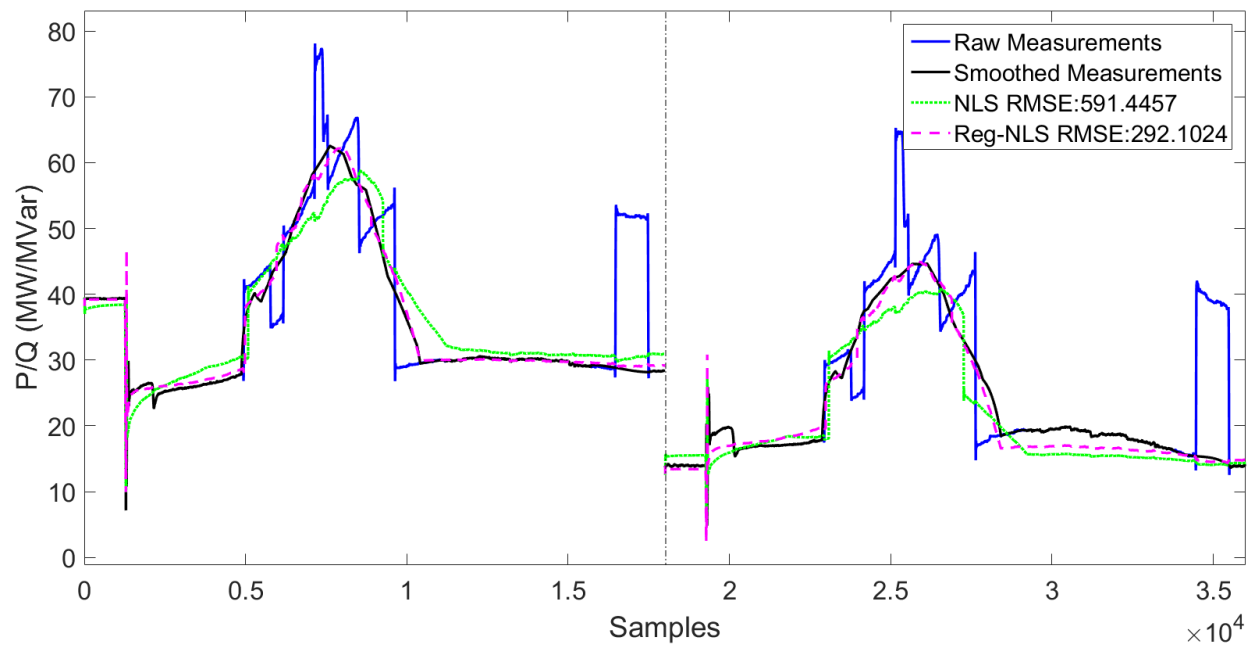
Figure 6.6: PQube dataset #1 with the fitting results attained by the NLS and regularized NLS methods.

Chapter 7

Conclusions

This work is focused on the complexity analysis of dynamic load models. Our proposed analysis used the trajectory sensitivity as the feature characterizing each parameter, and employed SVD and K-medoids to provide quantitative characterization and intuitive visualization of the CMPLDW parameters' interdependency, respectively. We found that the sensitivity of the parameters is dependent on the fault voltage profile, due to thresholding nonlinearity. Among sensitive parameters, some physically unrelated parameters were also shown to exhibit interdependency. The consequence of this unidentifiability is that a model which fits the training data can still perform poorly on other test cases. Increasing the number of training cases was also not beneficial. To tackle the identifiability issues for measurement-based load modeling, we developed two improved parameter estimation approaches based on the use of *a priori* information about the parameter values: the MAP estimator, and the 2-norm regularized estimator. Extensive numerical tests using both synthetic and real fault data have shown that both approaches result in significant improvements from the original NLS estimator, even under high noise conditions. This work shows that our improved measurement-based method can provide promising load modeling performance.

Part II

University of Wisconsin-Madison

Chapter 8

Introduction

8.1   Point-on-wave effects on compressor loads

The Fault-Induced Delayed Voltage Recovery phenomenon is believed to be driven by the stalling of compressor motors after a fault [25]. It is suggested that small compressor motors, with very low inertia, will stall after a very brief disturbance, even when the fault is properly cleared.In the desert southwest, FIDVR events are relatively common. A brief voltage disturbance can cause residential air conditioners to stall all along a feeder or substation, dragging down the voltage. After several seconds, the individual loads will trip off line by their own thermal protection, and the voltage will eventually rise. With the loss of a significant part of the load, the voltage rises above the pre-fault state, and network components (LTC, switched capacitors) react to lower the voltage. After several minutes the air conditioners will restart, lowering the voltage further.

This stalling characteristic of residential air conditioners has been confirmed in multiple laboratory experiments conducted by BPA, SCE, and EPRI. The air conditioners stall very quickly, and typically cannot overcome the compressor load to restart immediately after the disturbance.

From a reliability point of view, the concern is that a FIDVR event could cascade, either initially, right after a disturbance, or due to a poorly timed second event occurring when the voltage is already low and the system is vulnerable. To study the possibility of such cascades, researchers in WECC have developed models for compressor loads that have been implemented in traditional power system simulators including PSLF, PSEE, and PowerWorld. What is typically a single-phase phenomenon occurring at distribution level-voltages, must be modeled to suit positive sequence simulators to assess wider cascade potential.

A fundamental premise when developing a positive sequence simulation model is that the model does not depend on fast, sub-cycle phenomena. If it does, then the subcycle effects must somehow be incorporated into the positive sequence model. In Chapter 9, we investigate the effect of subcycle point-on-wave effects on single phase compressor motors.

8.2   Load monitoring

Improved dynamic load modeling is essential for predictive studies that examine the resilience of the network to any possible disturbance. The critical importance of accurate load models has been recognized since the 1996 blackouts in the Western Interconnect. An exhaustive post-blackout simulation study conducted by the WSCC could not reproduce the blackout event until improved dynamic load models were used. [26] This comprehensive analysis first determined all the control characteristics of generation at the time, and confirmed networks models. Nevertheless, the instability that drove the system to break up could not be replicated in simulation without the inclusion of load model dynamics, and a characterization of induction motors became standard in the West [27]. More recently, observation of Fault-Induced Delayed Voltage Recovery (FIDVR) event led efforts to develop a more detailed load model, culminating in the CMPLDW composite load model that is the new standard in WECC. This model has the fidelity to represent measured disturbance data in simulation.

The load characteristic is not fixed. Wide daily and seasonal variations are apparent in data. Figure 8.1 shows the MISO load for the year 2012, sampled hourly. The seasonal variations are obvious, with a strong peak in the summer, a lesser peak in the winter, and spring and fall lows. The summer peak is more than double the spring minimum. There is also great variability in load over the course of a day. Figure 8.2 shows a typical spring load characteristic in MISO in which the weekdays and readily observed. The daily variation is large; the range from low to high is approximately 20 % of the average load. Obviously the load types vary over the course of a day, by season, and by weather. On a hot summer day, the load will be dominated by air conditioner load (which explains more frequency FIDVR events in the summer in the Southwest). In other seasons the residential air conditioning load may be negligible. Commercial motor and lighting load will vary by time day, climate, season, etc.

The typical approach to developing a load model for a specified day/season/climate involves either a disaggregation of a load profile into percentage of individual load classes (industrial, agriculture, commercial, residential), or construction of a model from assumed percentages of the load classes. In either case the load class percentages are translated into parameters in a composite load model. To do this requires a lot of information about typical loads by location and climate. Much of this information comes from historical end-use load surveys, and can be correlated to utility billing data by type and substation. Using such databases, and expert knowledge, Pacific Northwest National Laboratories has developed a Load Modeling Data Tool (LMDT) that takes as input a bus location in the west, climate zone, time of year time of day, and percent load composition, and produces the parameters needed for the WECC CMPLDW composite load model [28].

Direct dynamic load measurement in real time is difficult, and just isn't done at the utility level. In Chapter 10, we look at how harmonic information can be used for load monitoring.
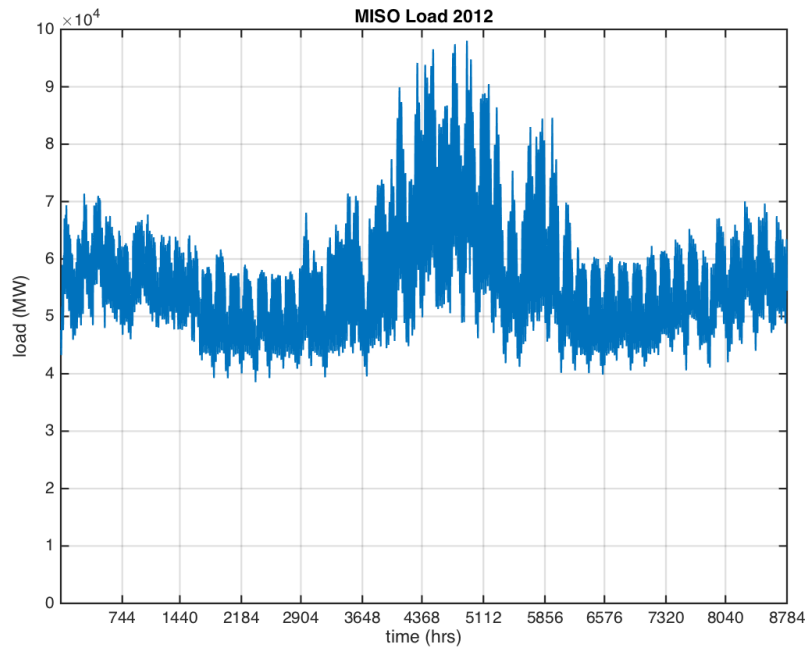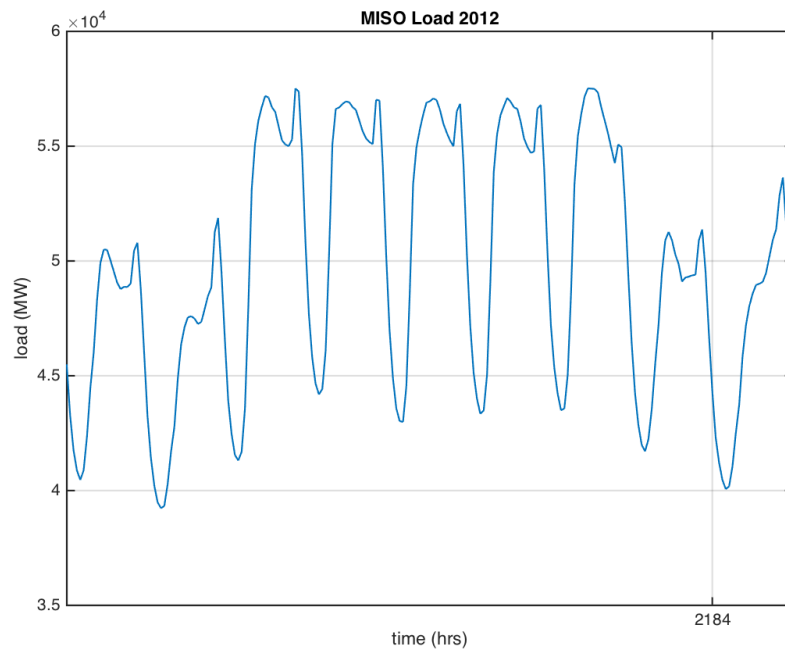
Figure 8.1: Total hourly MISO load for Year 2012.

Figure 8.2: Typical MISO spring load profile for nine days showing weekday and weekend variations.

Chapter 9

Point-on-Wave Effects on Compressor Loads

9.1   Compressor loads and point-on-wave Effects

We begin our study of the point-on-wave effects using simulations. We follow up in the next section with laboratory tests. The simulations use a textbook-type model of a two phase motor in which the second, or auxiliary winding, is connected to the main wind through a run capacitor as shown in Figure 9.1. We model mechanical load as triangle wave in angular displacement as a representation of a reciprocating compressor. We use the simulation model to determine the effect of the timing of the fault on the voltage wave to the stalling of the motor. We also assess the effect of the timing of the fault on the angular displacement of the motor on the stalling of the motor.
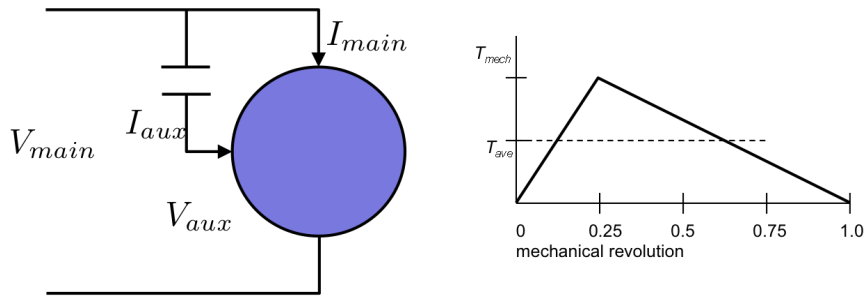
Reciprocating Compressor Mechanical Load

Figure 9.1: Diagram for single phase compressor simulations including mechanical torque.

A collection of typical voltage disturbances are shown in Figure 9.2. The applied voltages shown occur at the peak of the voltage waveform, the zero-crossing, and critical points in between. The results of these simulation collections are shown in Figure 9.3. This graph plots the simulated machine speed. It is clear that motor stalling *does depend on point-on-wave* effects. Disturbances occurring a the voltage peak, for this level of disturbance does not cause the motor to stall. Disturbances occurring at the zero-crossing does cause the motor to stall. In between there is a critical

angle for which the motor may or may not stall depending on the angular displacement in the compression cycle. Overall, this latter effect is small compared to the point-on-wave effect. One of the lines on the plot show a disturbance that just barely recovers, while a nearby line just fails to recover.
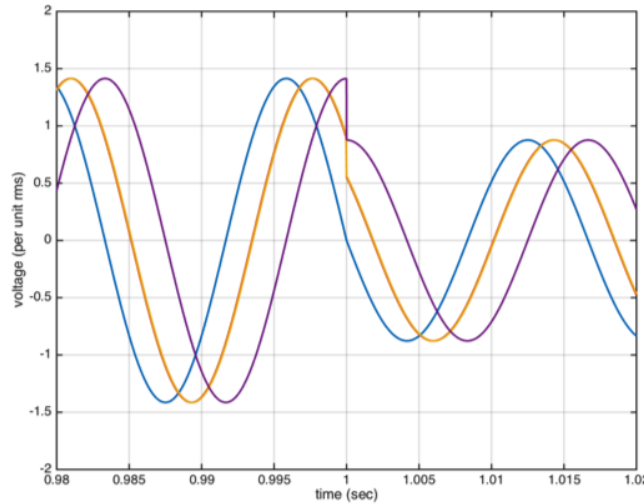

Figure 9.2: Collection of typical voltages used in simulations to show differences in point-on-wave application. They are distinguished by where on the voltage cycle the fault occurs: peak, zero crossing, in between.

When studying the impact of faults, it's usual to characterize the fault by its voltage dip and its duration. In Figure 9.4 we map out the space of stall characteristics as a function of fault duration (horizontal axis), maximum fault voltage that results in stall (vertical axis), with the lines representing simulations with faults starting at a peak, zero crossing and 45 degrees. The small distributions of points in the plots represent the effect of rotor position at the time of disturbance, which turns out to be a small and negligible effect. In this plot, the lower curves are better. They show that the motor is able to withstand a larger voltage dip during the fault without before stalling. The zero-crossing points are most sensitive to the voltage dip, and the voltage peaks values are the least sensitive.

For studying fault-induced delayed voltage recovery, a primary question is whether a disturbance is likely to spread. At the location of a fault the voltage disruption can be abrupt as simulated above. That is, we have treated the voltage change to be instantaneous. At some electrical distance away, filtered by transformers, lines, and with (limited) energy and power support from other devices, the waveform may be smoothed slightly. Assuming that at some distance away from the fault the voltage disturbance may appear very slightly smoothed, we performed a set of simulations and tests to examine how sensitive the stall results are to a smoothing of the waveform. We repeated the simulations and tests by imposing a one-cycle ramp in the voltage disturbance. A sample voltage disturbance waveform with a 1 cycle ramp is shown in Figure 9.5. The simulation

44

and test results are shown in Figure 9.6 respectively. These results show that the point-on-wave effect is significantly mitigated by the 1-cycle ramp.

For the objective of developing load models for system wide studies, the results of the 1-cycle smoothing simulations and laboratory tests are helpful. They suggest that detailed point-on-wave simulations may not be necessary to study FIDVR phenomena. For loads at the point of disturbance which may experience instantaneous changes in voltages, the voltage will likely be low enough to initiate stall even if a 1-cycle voltage smooth is assumed. For determining whether an event is likely to spread the 1-cycle smoothing will allow quasi-static phasor simulations. Furthermore it is noted in practice that FIDVR events do not tend spread. The smoothing results suggest a reason for this, that even a small amount of smoothing reduces the chance of stalling under the worst-case point-on-wave initiating event.

9.2   Laboratory tests of point-on-wave effects.

The simulation results suggest that for instantaneous voltage changes, the point-on-wave effect can be substantial. The compressor may or may not stall depending on the sub-cycle timing of the disturbance. However, when the voltage waveform is slightly smoothed, this effect is greatly lessened. Then the point-on-wave effect is small, and may be considered negligible for purposes of developing a simulation model.

It is necessary to test these results in a laboratory environment. We conducted a suite of tests on two types of air conditioners at the test facilities at the Bonneville Power Administration in Vancouver, WA. This included a scroll compressor, and a reciprocating compressor. The purpose of the tests to examine both the effects of point-on-wave for instantaneous disturbances and for 1-cycle smoothed disturbances.

Figures 9.7 and 9.8 summarize the stall characteristics as a function of voltage dip, fault duration, and point-on-wave, for the scroll compressor tested at the BPA facility. Figure 9.7 uses and instantaneous voltage disturbance and Figure 9.8 uses a 1 cycle smoothed voltage disturbance. It is clear that the qualitative conclusions suggested by the simulations are confirmed by the laboratory tests. The point-on-wave effect does matter for instantaneous voltage events but is greatly mitigated by smooth the voltage.

This same conclusion is drawn from the tests of the reciprocating compressor tests. The results of those tests are summarized in Figures 9.9 and 9.10
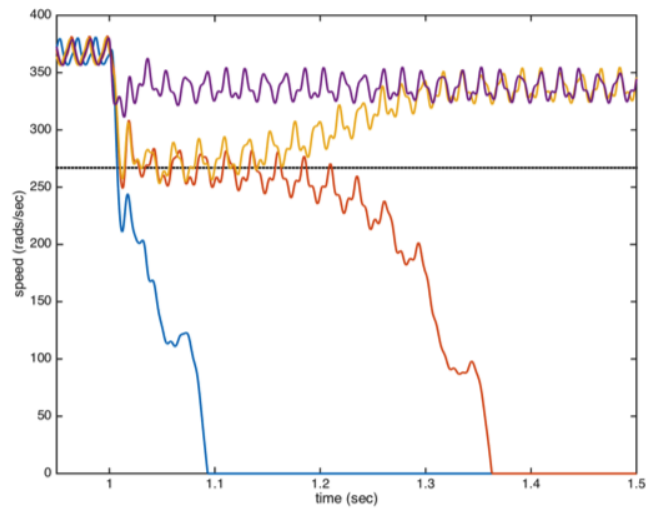
Figure 9.3: Collection of simulated machine speeds shown the effect of point-on-wave application of disturbance. Simulations suggest that disturbances occurring at a zero-crossing of voltage will be more likely to stall than those occuring at a peak.
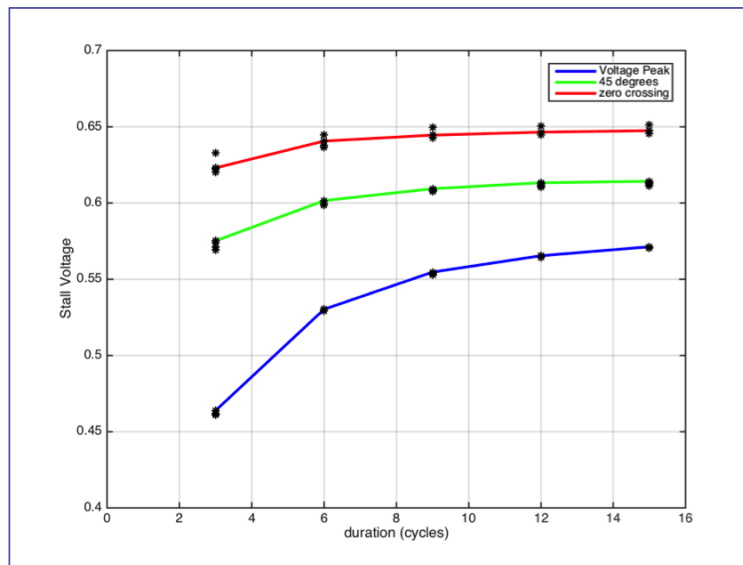

Figure 9.4: Voltage Dip vs. fault duration for compressor stalling as a function of point-on-wave.
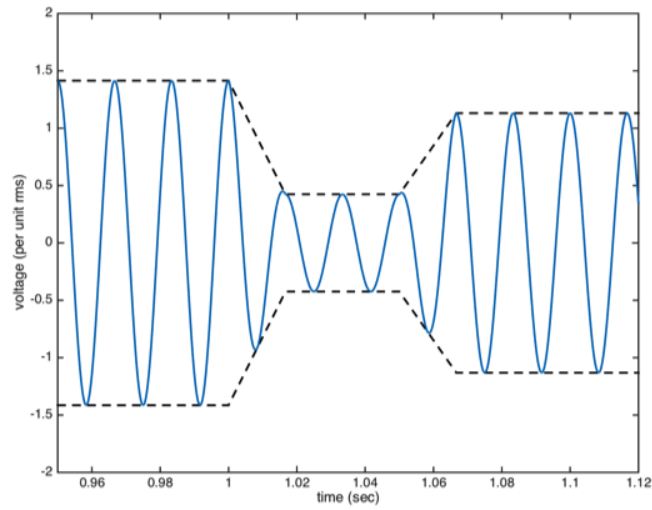
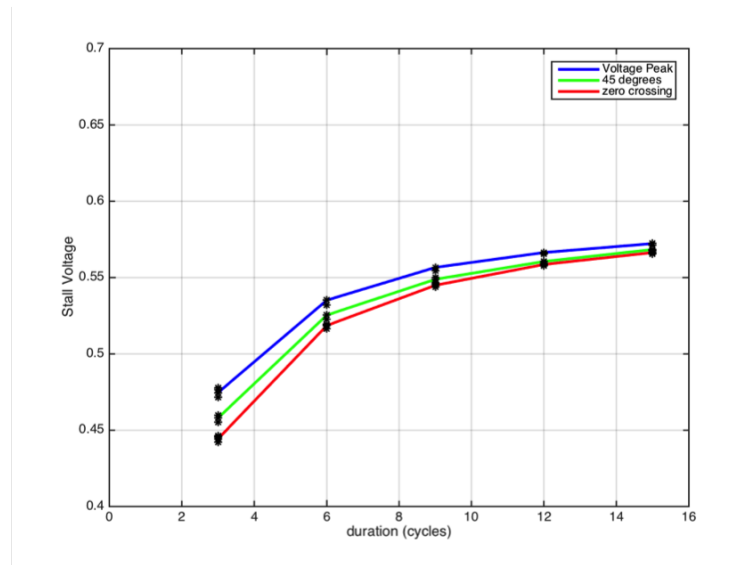Figure 9.5: A sample voltage disturbance smoothed over one cycle.

Figure 9.6: Voltage Dip vs. fault duration for compressor stalling as a function of point-on-wave with a 1 cycle ramp. The ramp greatly reduces the point-on-wave effect.
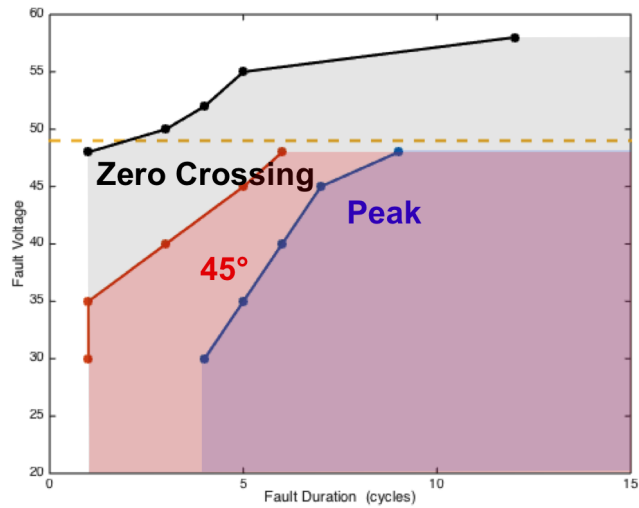
Figure 9.7: Voltage Dip vs. fault duration for scroll compressor stalling as a function of point-on-wave. The disturbance is instantaneous, i.e. no smoothing ramp.

Figure 9.8: Voltage Dip vs. fault duration for scroll compressor stalling as a function of point-on-wave. The disturbance voltage is smoothed with a 1 cycle ramp.

Figure 9.9: Voltage Dip vs. fault duration for reciprocating compressor stalling as a function of point-on-wave. The disturbance is instantaneous, i.e. no smoothing ramp.
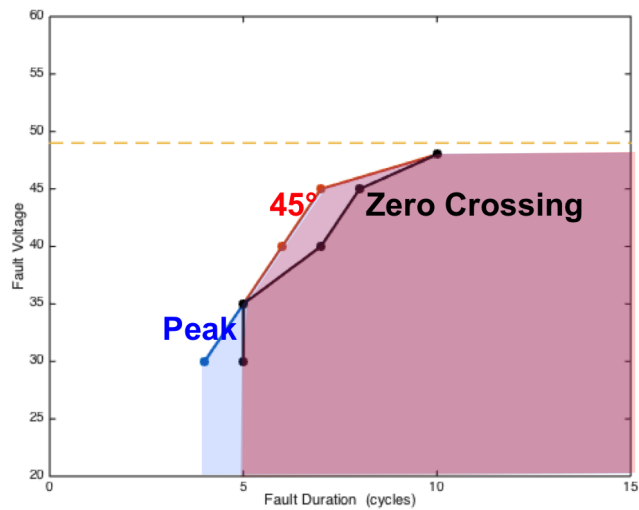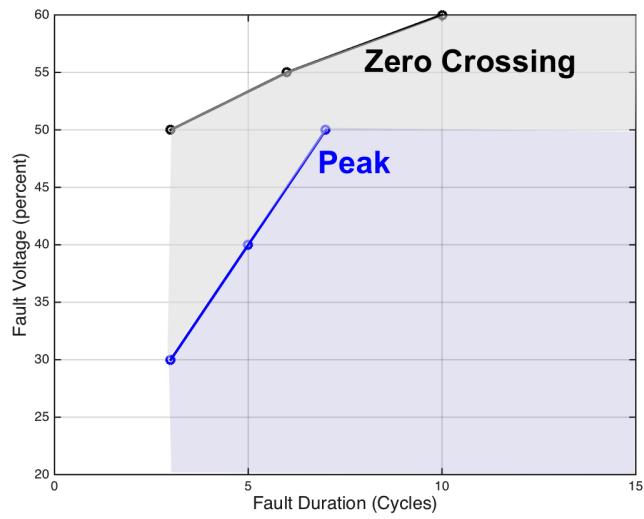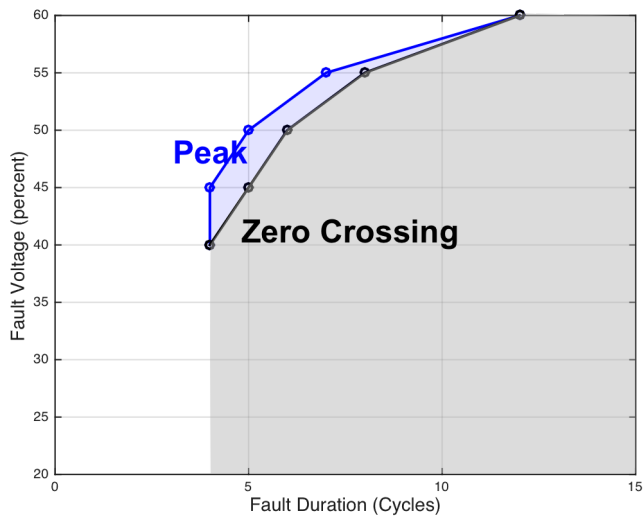

Figure 9.10: Voltage Dip vs. fault duration for reciprocating compressor stalling as a function of point-on-wave. The disturbance voltage is smoothed with a 1 cycle ramp.

Chapter 10

Load Monitoring

10.1   Load monitoring using harmonic information

In this section we discuss one method for direct measurement of load types that may be applied in real time. This approach relies on gathering high bandwidth electrical data.

One of the challenges with estimating parameters of a dynamic model from measurements is that the data must be excited in some way to reveal the dynamic behavior. From disturbance data, one can calibrate model parameters, as is discussed earlier in this report. It is more difficult to determine model dynamics when the model shifts slowly over time. In this section we suggest that there is a different approach that may reveal something about the nature of the load using steady state measurements of harmonic information. While in steady state it would be difficult to discern differences between loads or even load types, it may be possible to detect characteristics of one important load type: power electronic loads [29].

Power electronic loads are typically characterized by a front-end rectifier that converts the AC source voltages and currents to a DC voltage and current that is then used directly, or is converted back to a different AC signal depending on the load. One increasingly common power electronic load is the variable frequency drive, which is of the latter type. By the nature of the rectifier circuit comprising diode bridges, the current waveform as seen by the grid will contain harmonics, unless special filtering components are added to the circuit. In Figure 10.1, the current on one phase of a three phase variable frequency drive is shown. These tests were conducted with the Bonneville Power Administration as part of past work on studying the characteristics of air conditioning load. The current displays typical "rabbit ears" that translate into strong 5th and 7th harmonics in current.

The question is whether such harmonics associated with power electronic rectified loads can be observed in an aggregate load. The challenge for examining this question is that the sampling rate must be very high to capture. Suppose we sample at 10000 Hz and saved all the data; one 16-bit data stream over one day would require more than a gigabyte of data. This adds up quickly, and one can easily understand why high-bandwidth data is not routinely collected. Before suggesting that such data should be collected, or at least the tracking of harmonics over time, sampled at some frequency, it is worth examining whether such harmonic characteristics can be seen in real data. Data at that bandwidth is collected when there is a disturbance, for some period before and after
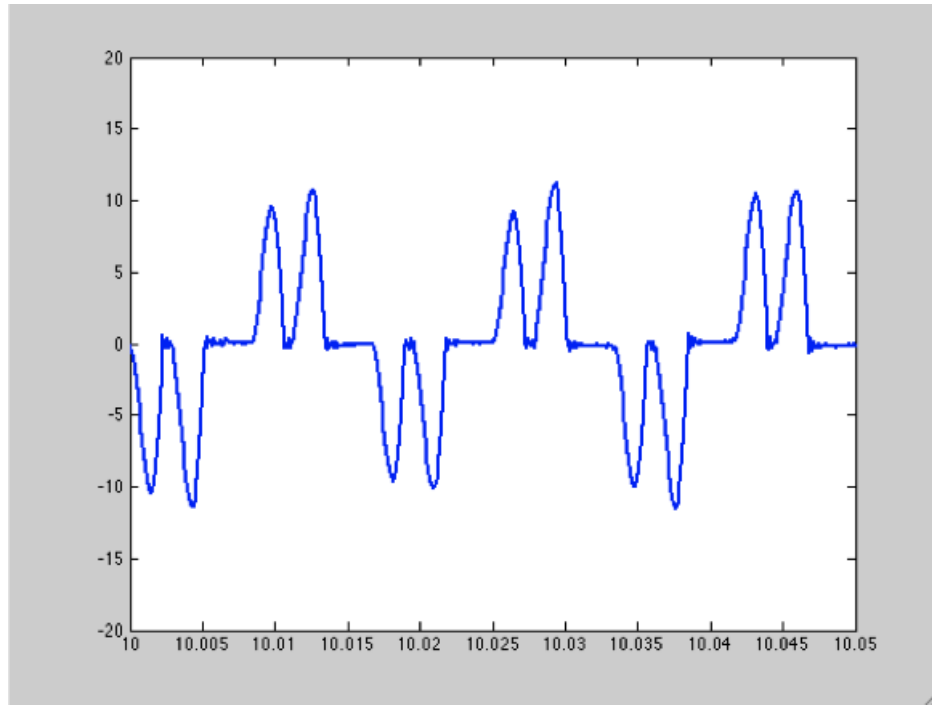
Figure 10.1: Source current on one phase of a three phase variable frequency drive. This current exhibits typical "rabbit ears", with strong fifth and seventh harmonics.

then event.

Researchers at Lawrence Berkeley National Laboratory have installed distribution-level phasor measurement units at various locations around their facility, specifically PQube devices (pqube.com). These devices will record point-on-wave measurements when there is a disturbance. A sample event is shown in Figure 10.2. The measurement was taken at the service entry of one the laboratory's building. The load in this building should be taken as a typical office building, and not one of the research building housing unique loads (such as high-powered lasers, or a supercomputer). A close examine of the current waveform suggests that there are likely harmonics. In our case, we are less interested in a detailed analysis of the dynamics, but rather on the harmonics in the steady state waveform. There is sufficient data and the end of the event detection to enable a harmonics analysis of the current in near steady state.

An FFT analysis for the current after 100ms, i.e., essentially steady state, is shown in Figure 10.3. The FFTs for each of the three currents are normalized by the magnitudes of their (peak) values at 60 Hz. This normalization allows easy comparison of harmonics relative to the fundamental frequency component. The odd-numbered harmonics are prominent at 180, 300, 420, 540, 660, and 780 Hz. Beyond the thirteenth harmonic the harmonics are essentially zero, possibly the result of an anti-aliasing filter in the system. There are noticeable differences in the amount of various harmonics. The third harmonic is almost 10% of the fundamental on one phase, and nearly absent on another. The differences in harmonic content suggests that the loads connected to the circuits are different.
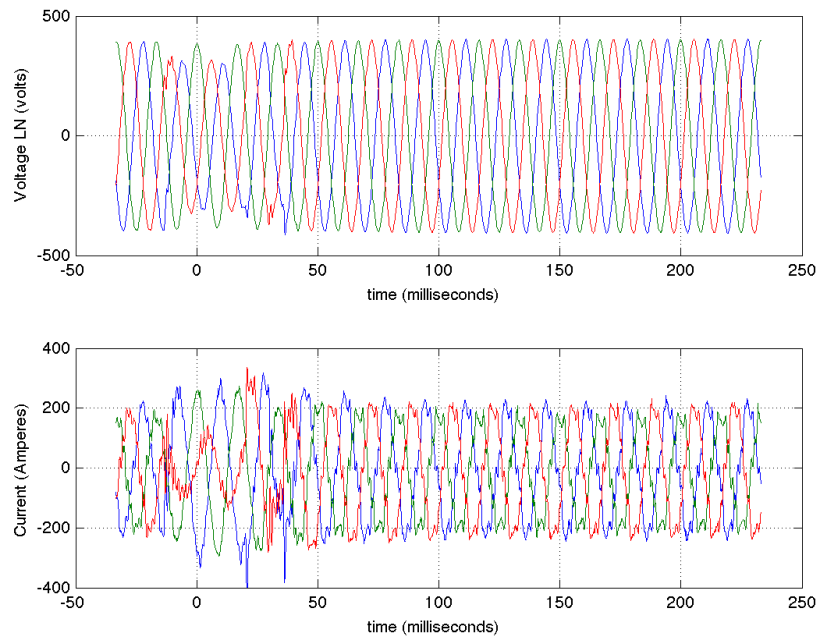
51

Figure 10.2: Recorded line-to-line voltages and currents.

10.2   Two weeks of monitoring harmonics

The data from the event records suggested that collecting steady-state harmonic information from electrical waveforms could be useful for identifying the part of the load associated with power electronic rectifiers. To this end we requested of a researcher at LBNL and the manufacturer of the PQube devices to alter the firmware for one devices to record 16 cycles of steady-state waveforms of voltage and current at 128 samples per cycle (7680 Hz), every hour for one week. We collected this data for waveforms into an office building at Lawrence Berkeley National Laboratory every hour for 317 hours (almost two weeks). A plot of harmonics is shown below in Figure 10.4. It is clear that there is substantial change (increase) in fifth and seventh harmonics during business hours on weekdays. On the first weekend there is very little harmonic activity, on the next week there is some. Checking with facilities confirms there was activities at the lab on that weekend, but not the prior weekend.

Looking at the harmonics in the current over the course of a day in Figure 10.5, suggests that there may be dominant load with a power electronic rectifier front end that turns on during the day, and off at night. The hypothesis that the building has HVAC equipment run by variable frequency drives was confirmed with facilities.

Looking at the time-domain point-on-wave characteristics for a sample during the afternoon in Figure 10.6 clearly shows "rabbit ears" consistent with a three phase power electronic rectifier. The amount observed depends on the time of day. It is obviously present in the afternoon, but is smaller or missing in the early morning. This comparison is shown in Figure 10.7.
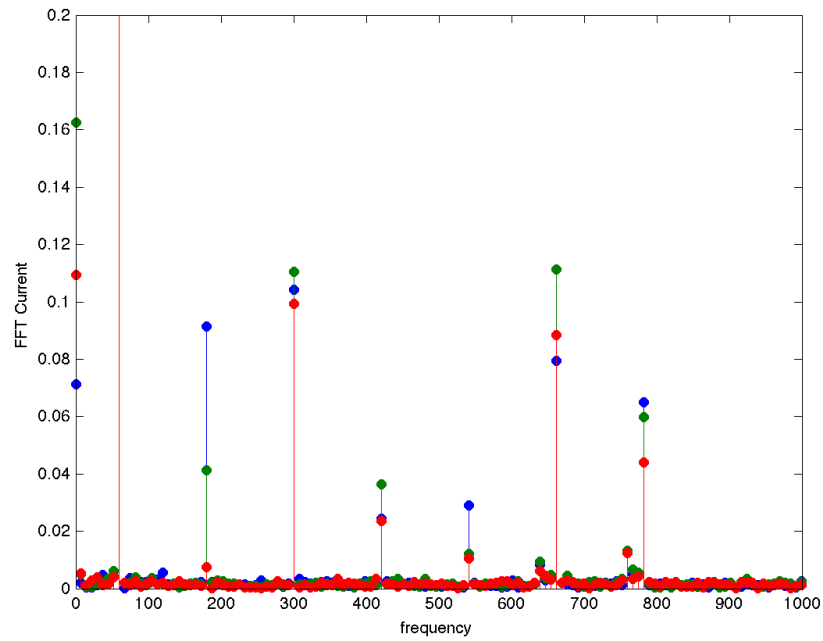
52

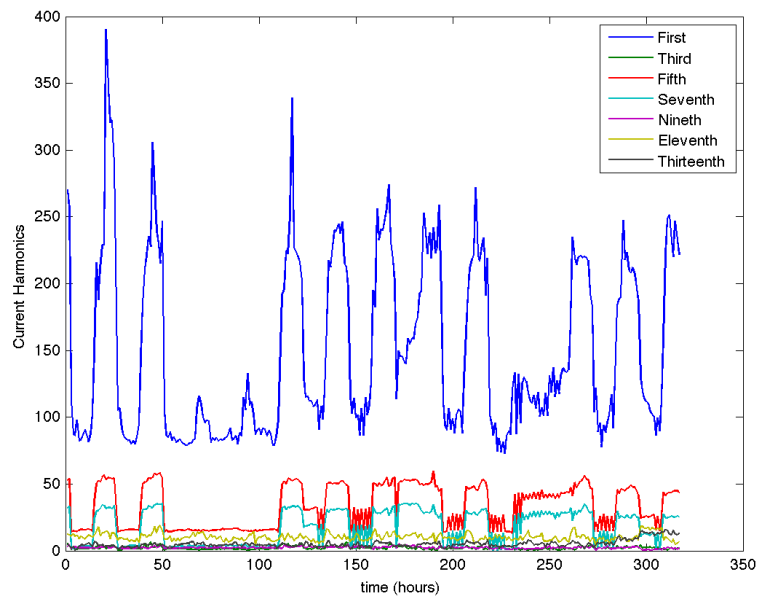Figure 10.3: FFT Analysis of Current Waveforms.

Figure 10.4: Plot of harmonics in current at the service entry of an office building at LBNL, recorded every hour for approximately two weeks. The harmonic content clearly changes over the course of a day.

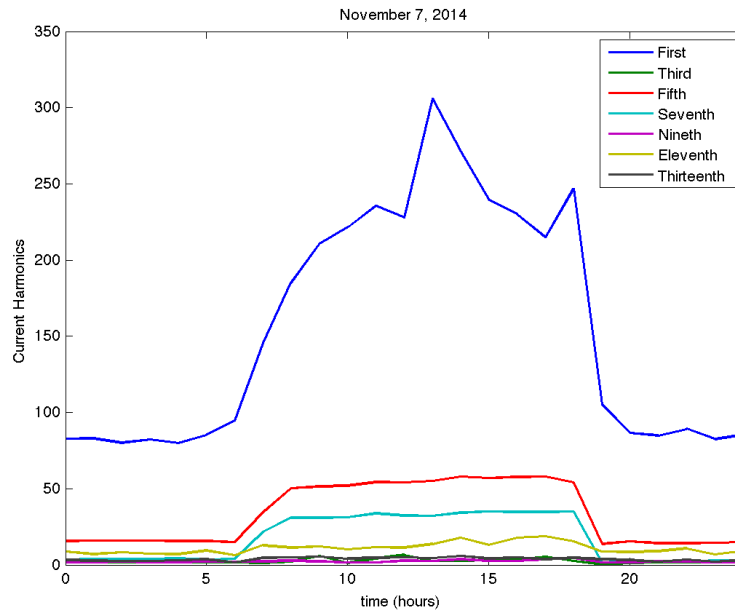Figure 10.5: Plot of harmonics in current at the service entry of an office building at LBNL, every hour for one day. The harmonic content changes suggest a dominant power electronic load, which we confirmed to drive HVAC equipment.
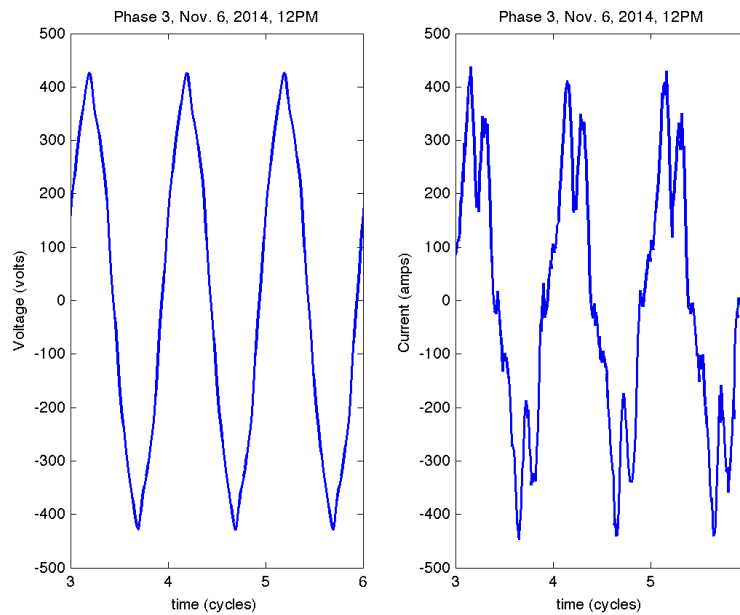

Figure 10.6: Plot of voltage and current observed in the afternoon. The current displays rabbit ears consistent with a power electronic rectified front-end to a load.
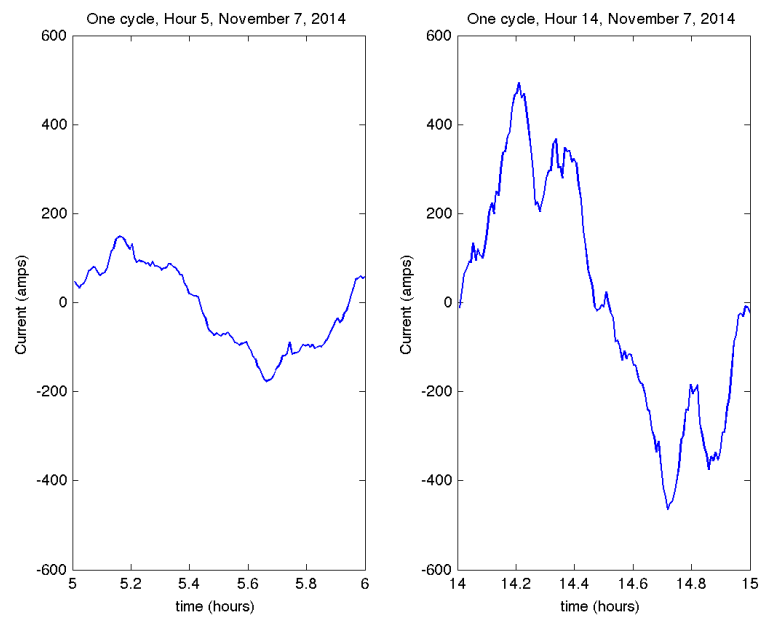
Figure 10.7: Comparison of current plots in the early morning and early afternoon. The distortion appears more pronounced in the afternoon.

Chapter 11

Conclusion and Future Work

11.1   Point-on-wave effects on compressor loads

In summary, understanding the point-on-wave effects are essential for modeling the FIDVR phenomenon in positive sequence simulators. It appears that the effect is small if the voltage disturbance is very mildly smoothed, in which case a model can be developed for use in a positive sequence simulator for the purpose of assessing the risk of cascading outages away from the point of disturbance. For the initiating event, at the point of disturbance, it still may be useful to modify the simulation model at that location to incorporate the effect of an instantaneous voltage event. The form of modification is a topic of further research.

11.2   Load monitoring

The data in Chapter 10 were collected on a one-time basis as the sensing equipment is not normally set up to gather information in this way. We were given two weeks to divert the normal use of these sensor for our purposes, from that of another LBNL project. We are grateful to have that opportunity. We did not have resources to survey the types of loads for the complete office building, which would have enabled the calibration of the measurements to percentage of power electronic loads, and to distinguish between single-phase and three-phase power electronics. We recommend that a subsequent study focus on installing a dedicated sensors for this purpose, along with resources for a (near) complete survey of loads for calibration.

Bibliography

[1] Maurice Kent, Wayne Schmus, Francis McCrackin, and Luther Wheeler. Dynamic modeling of loads in stability studies. *IEEE Trans. Power Appar. Syst.*, PAS-88(5):756–763, 1969.

[2] John Adiaz De Leon and Bud Kehrli. The modeling requirements for short-term voltage stability studies. In *Proc. IEEE PES Power Syst. Conf. Expo.*, pages 582–588, Oct. 2006.

[3] Ian A. Hiskens and Jassim Alseddiqui. Sensitivity, approximation, and uncertainty in power system dynamic simulation. *IEEE Trans. Power Syst.*, 21(4):1808–1820, 2006.

[4] Jin Ma, Dong Han, Renmu He, Zhaoyang Dong, and David J. Hill. Reducing identified parameters of measurement-based composite load model. *IEEE Trans. Power Syst.*, 23(1):76–83, 2008.

[5] Byoung-Kon Choi and Hsiao-Dong Chiang. Multiple solutions and plateau phenomenon in measurement-based load model development. *IEEE Trans. Power Syst.*, 24(2):824–831, 2009.

[6] Seoeun Son, Soo-Hyoung Lee, Dong-Hee Choi, Kyung-Bin Song, Jung-Do Park, Young-Hoon Kwon, Kyeon Hur, and Jung-Wook Park. Improvement of composite load modeling based on parameter sensitivity and dependency analyses. *IEEE Trans. Power Syst.*, 29(1):242–250, 2014.

[7] Jae-Kyeong Kim, Kyungsung An, and Jin Ma. Fast and reliable estimation of composite load model parameters using analytical similarity of parameter sensitivity. *IEEE Trans. Power Syst.*, 31(1):663–671, 2016.

[8] Siming Guo and Thomas J Overbye. Parameter estimation of a complex load model using phasor measurements. In *Proc. Power & Energy Conf. at Illinois*, pages 1–6, Feb. 2012.

[9] Dmitry Kosterev, Anatoliy Meklin, John Undrill, Bernard Lesieutre, William Price, David Chassin, Richard Bravo, and Steve Yang. Load modeling in power system studies: WECC progress update. In *Proc. IEEE PES Gen. Meet.*, Jul. 2008.

[10] Alex Borden and Bernard Lesieutre. Model validation: FIDVR event. Technical report, University of Wisconsin-Madison, Madison, WI, 2009.

[11] Isen Widjaja, Dean Latulipe, Daniele D'Aquila, Gene Ng, and Khin Swe. SS-38 load modeling working group progress report. Technical report, NERC, 2016.

[12] Leonard Kaufman and Peter J Rousseeuw. Partitioning around medoids. In *Finding Groups in Data*, pages 68–125. Wiley-Interscience, 1990.

[13] P Bickel, P Diggle, S Fienberg, U Gather, I Olkin, S Zeger, Alho Spencer, and Statistical Demography. *Modern Multidimensional Scaling Theory and Applications*. Springer, New York, NY, 2nd edition, 2010.

[14] Siemens Inc. PSS/E 33.0 Model Library, 2011.

[15] PowerWorld Corporation. Block diagrams, 2015.

[16] Power Standards Lab. *PQube installation and user manual*, 2015.

[17] Siming Guo and Thomas J Overbye. Suitability of a dynamic load model to measurement-based parameter estimation. In *17th International Conference on Intelligent Systems Application to Power Systems*, 2013.

[18] I.a. Hiskens and M.a. Pai. Trajectory sensitivity analysis of hybrid systems. *IEEE Trans. Circuits Syst.*, 47(2):204–220, 2000.

[19] M. Grewal and K. Glover. Identifiability of linear and nonlinear dynamical systems. *IEEE Trans. Auto. Contr.*, 21(6), 1976.

[20] G. H. Golub and C. F. Van Loan. *Matrix Computations*. The Johns Hopkins University Press, 3rd edition, 1996.

[21] Peter J. Rousseeuw. Silhouettes: A graphical aid to the interpretation and validation of cluster analysis. *J. Comput. Appl. Math.*, pages 53–65, 1987.

[22] J.D. Glover, M.S. Sarma, and T.J. Overbye. *Power System Analysis and Design*. Thomson Learning, Stamford, CT., 5th edition, 2008.

[23] Bruce Hajek. *Random Processes for Engineers*. Cambridge University Press, Cambridge, 1 edition, 2015.

[24] Mark K. Transtrum and James P. Sethna. Improvements to the Levenberg-Marquardt algorithm for nonlinear least-squares minimization. unpublished, 2012.

[25] NERC Load Modeling Task Force. Technical Reference Document: Dynamic Load Modeling. Technical report, North American Electic Reliability Corporation, December 2016.

[26] Dimitry N. Kosterev, Carson W. Taylor, and William A. Mittelstadt. Model Validation for the August 10, 1996 WSCC System Outage. *IEEE Trans. Power Syst.*, 14(3):967–979, 1999.

[27] Les Pereira, Dmitry Kosterev, Peter Mackin, Donald Davies, John Undrill, and Wenchun Zhu. An interim dynamic induction motor model for stability studies in the WSCC. *IEEE Trans. Power Syst.*, 17(4):1108–1115, 2002.

[28] David Chassin and Pavel Etingov. Load Model Data Tool. Technical report, Pacific Northwest National Laboratory: https://svn.pnl.gov/LoadTool, 2013.

[29] Steven B. Leeb, Bernard C. Lesieutre, and Steven R. Shaw. Determination of Load Composition using Spectral Envelope Estimates. In *Proc. 1995 North American Power Symposium*, pages 618–627, October 1995.